Drift-Diffusion Simulation of the Ephaptic Effect in the Triad Synapse of the Retina

by

Jeremiah Jones

A Dissertation Presented in Partial Fulfillment
of the Requirements for the Degree
Doctor of Philosophy

Approved April 2013 by the
Graduate Supervisory Committee:

Carl Gardner, Chair
Steven Baer
Sharon Crook
Eric Kostelich
Christian Ringhofer

ARIZONA STATE UNIVERSITY

May 2013

ABSTRACT

A general continuum model for simulating the flow of ions in the salt baths that surround and fill excitable neurons is developed and presented. The ion densities and electric potential are computed using the drift-diffusion equations. In addition, a detailed model is given for handling the electrical dynamics on interior membrane boundaries, including a model for ion channels in the membranes that facilitate the transfer of ions in and out of cells. The model is applied to the triad synapse found in the outer plexiform layer of the retina in most species. Experimental evidence suggests the existence of a negative feedback pathway between horizontal cells and cone photoreceptors that modulates the flow of calcium ions into the synaptic terminals of cones. However, the underlying mechanism for this feedback is controversial and there are currently three competing hypotheses: the ephaptic hypothesis, the pH hypothesis and the GABA hypothesis. The goal of this work is to test some features of the ephaptic hypothesis using detailed simulations that employ rigorous numerical methods. The model is first applied in a simple rectangular geometry to demonstrate the effects of feedback for different extracellular gap widths. The model is then applied to a more complex and realistic geometry to demonstrate the existence of strictly electrical feedback, as predicted by the ephaptic hypothesis. Lastly, the effects of electrical feedback in regards to the behavior of the bipolar cell membrane potential is explored. Figures for the ion densities and electric potential are presented to verify key features of the model. The computed steady state IV curves for several cases are presented, which can be compared to experimental data. The results provide convincing evidence in favor of the ephaptic hypothesis since the existence of feedback that is strictly electrical in nature is shown, without any dependence on pH effects or chemical transmitters.

ACKNOWLEDGEMENTS

I would like to express my deepest gratitude to my advisor and mentor, Carl Gardner. His constant guidance, support, insight and patience has been a resource of enormous magnitude to me and this research would not have been possible without him.

I am also deeply grateful to Steven Baer, Sharon Crook, Shaojie Chang and Maarten Kamermans for all of their invaluable advice with regard to the neuroscience modeling aspects of my research.

I also give thanks to Eric Kostelich, who served as an influential mentor to me as an undergraduate in the CSUMS program and inspired me to pursue graduate studies in computational mathematics.

A special thanks also goes to Dirk Gillespie for agreeing to be the official outside reader for this thesis and for offering very valuable feedback.

I would like to thank the School of Mathematical & Statistical Sciences at ASU for their invaluable financial and professional support. In particular, a special thanks goes to the Graduate Program Coordinator, Debbie Olsen, who does such a wonderful job in helping us students get through the program.

I would like to thank the National Science Foundation for partially funding my research under grant DMS-0718308 and for their continued dedication to the advancement of science.

Finally, I would like to express my deepest thanks to all my family and friends for their support and encouragement.

TABLE OF CONTENTS

LIST OF TABLES

LIST OF FIGURES

Figure Page

Chapter 1

INTRODUCTION

1.1 Nervous Systems

Nervous systems are highly complex networks of communicating cells, called neurons, that are found in most multicellular organisms. The nervous system has multiple functions that are key to survival of the organism, including sensory perception and controlling movement and balance. The development of the nervous system was a key evolutionary step in the emergence of complex organisms and is considered to be one of the most complex systems known to science. In most organisms, the nervous system is separated into two parts: the central nervous system and the peripheral nervous system. The peripheral nervous system consists of sensory and motor neurons. Sensory neurons detect stimuli from the outside environment (heat, pressure, light, etc.) and motor neurons are responsible for the organism's reaction to the stimuli. The central nervous system contains neurons referred to as integrators, which receive input signals from sensory neurons and send appropriate responses to the motor neurons. The central and peripheral nervous systems are connected through bundles of nerve fibers held together by connective tissue, which allows rapid communication between individual neurons.

Anatomy of Neurons

Figure 1.1 shows a diagram of the anatomy of a typical neuron. The main substructures found in neurons are the cell body (or soma), the dendrites (or processes) and the axon. The soma resembles a typical cell in function and form. It is surrounded by a plasma membrane and contains a nucleus, along with other common cellular organelles. Dendrites resemble branched structures that extend from the soma and they are responsible for receiving electrical input from other neurons. The axon is a long cable-like structure that extends away from the soma at a junction called the axon hillock. At the end of the axon, branched structures called axon terminals come into close proximity with the dendrites of other neurons. When dendrites receive

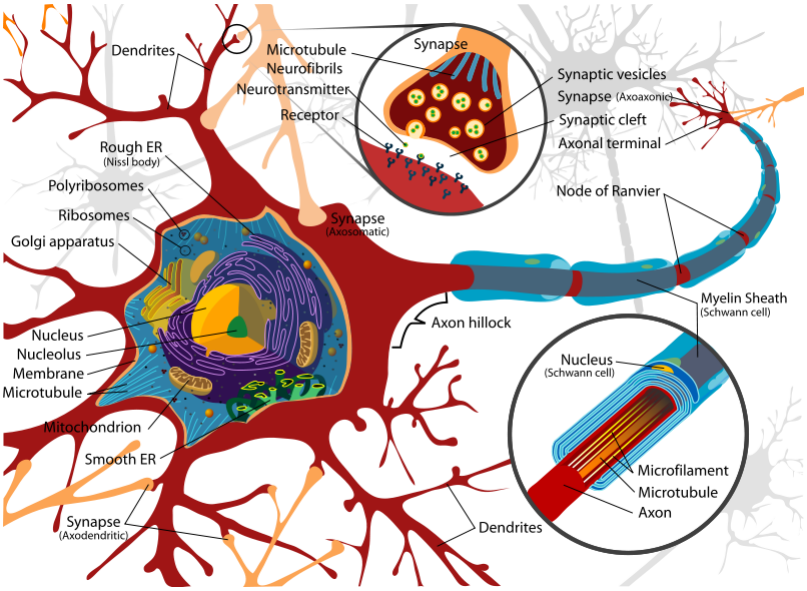

Figure 1.1: Detailed diagram of a neuron and chemical synapse [47].

electrical input, the signal propagates down the axon to the axon terminals, which then provide input to the dendrites of connected neurons. A given neuron may be connected to hundreds or thousands of other neurons and the cell bodies of connected neurons need not be close in proximity given that axons can be up to meters in length.

Neurotransmission

The communication between neurons, referred to as neurotransmission, takes place at regions called synapses, which are either electrical or chemical. The cell producing the signal is called the pre-synaptic cell and the cell receiving the signal is called the post-synaptic cell. An electrical synapse, also called a gap junction, is a channel that directly connects the cell bodies of two neurons, allowing rapid transfer of electric charge between the cells. Chemical synapses are the regions where the dendrites from one neuron come into close proximity with the axon terminals of another neuron and are separated by a small gap of about 20-40 nanometers as shown in the upper magnified region of Figure 1.1. In a chemical synapse, electric signals propagate down the axon and upon reaching the axon terminal, stimulate the cell membrane to open vesicles containing chemical messengers, called neurotransmitters. These neurotransmit-

ters then diffuse across the intersynaptic space (or synaptic cleft) and bind to receptor proteins in the post-synaptic cell. The reception of the neurotransmitters in the post-synaptic cell triggers the cell to either open or close ion channels in the cell membrane, which can control the flow of electric current into or out of the cell. Note that electrical synapses operate on much faster time scales than chemical synapses. There is also a more subtle form of communication between neurons, known as ephaptic coupling. This can occur when the ion channels of two neighboring cells are in close proximity. The flow of ions through channels of one cell can cause local changes in the extracellular electric potential, which can be sensed by the channels of the neighboring cell. As we will see, this study is largely concerned with investigating a specific instance of ephaptic coupling.

1.2 Membrane Potential

All cells are surrounded by and filled with a biological fluid, which is mostly water. The polarized nature of water causes ionic salts to dissociate their ions. It is the movement of these ions that provides the electrical current used by the nervous system. The four main ions that play a significant role in the nervous system are Na^+, K^+, Ca^{2+}, and Cl^-, although there are other less common ions that can play a role as well. When the quantity of ionic charge inside a cell is different than it is outside the cell, there is a net potential difference across the cell membrane, referred to as the membrane potential, usually denoted as V_m in the literature. By convention, $V_m = \phi^+ - \phi^-$ where ϕ^+ is the intracellular potential and ϕ^- is the extracellular potential. Although every cell has a membrane potential, one of the distinguishing features of neurons is that they are excitable, i.e., they have the ability to drastically alter their membrane potential through the use of ion channels.

Ion Channels

An ion channel is a complex protein structure found in the membranes of cells that acts as a gate to allow ions to pass into or out of the cell. Ion channels come in a wide variety of

forms. Some channels show a high degree of selectivity, i.e., they can only be used by certain types of ions while others are more passive. For instance, the channel may have a narrow filtering region that will not allow large ions to get through. In addition, many channels come with immobile charges embedded in the protein structure, often referred to as "background" charge, that create a static electric field that is favorable to ions of a certain charge, analogous to doping in semiconductors. There are some channels that always remain open (non-gated), but more commonly they have complex mechanisms that control the process of opening (activation) and closing (inhibition). In a voltage-gated channel, the open/closed state is controlled by the membrane potential. These channels remain closed until the membrane potential reaches a particular threshold value that triggers them to open. Once the necessary charge is exchanged, the membrane potential falls below the threshold value and the channels return to a closed state. There are also channels with gating mechanisms controlled directly by neurotransmitters, as in a chemical synapse. The binding of the neurotransmitter to the membrane signals these channels to either open or close, depending on the nature of the neurotransmitter and the type of channel. A simple schematic of a typical channel is shown in Figure 1.2. The green charges show the ions that are permeable to the channel, the black and white charges show the immobile background charge and the dashed lines around the openings are isopotentials. For a complete treatment of the subject of ion channels, see [20].

Resting Potential

Every cell membrane has a resting potential in which the intracellular and extracellular charge balances in such a way that no current will flow. The resting potential for a typical neuron is about -70 mV although this value can vary considerably depending on the function of the neuron. This suggests that at rest, $\phi^+ < \phi^-$, i.e., there is more positive charge outside the neuron than inside. When ion channels allow the flow of positive charge into the neuron, the membrane potential is increased toward zero (depolarized). Alternatively, if the channel allows positive charge to flow out of the neuron, the membrane potential is decreased to a more negative value (hyperpolarization).

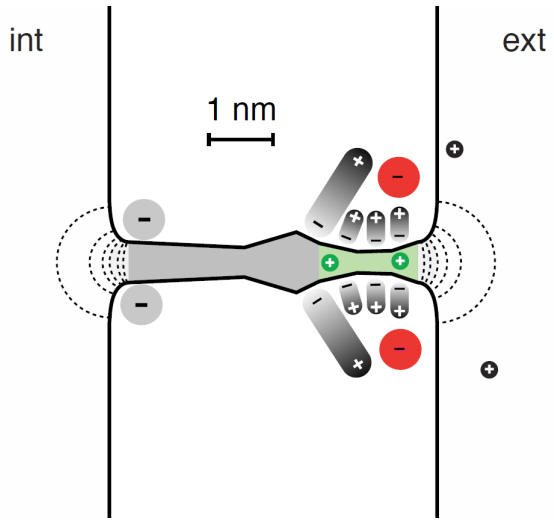

Figure 1.2: Schematic of an ion channel [17].

The Circuit Model

Since the bilipid layers of cellular membranes are poor electrical conductors, charge will accumulate on their surfaces much like a capacitor in an electrical circuit. The current passing through the ionic channels can thus be viewed as capacitive current. This suggests that a patch of membrane can be modeled with an equivalent electrical circuit, as shown in Figure 1.3. The parallel resistors represent the individual ion channels with sodium and potassium as variable resistors, i.e., their conductance is a function of the membrane potential. Note that there is also a "leak" current which is meant to account for the miscellaneous forms of current through the membrane. Each resistor has a corresponding battery, labeled by E_i, which represents the resting potential of the ion. The value of C_m is the membrane capacitance per unit area, which has been measured to be approximately 1 μF/cm^2 for a typical neuron. This equivalent circuit model has enjoyed much success in theoretical neuroscience although it still remains a challenge to researchers on how to model the conductance functions for the variable resistors.

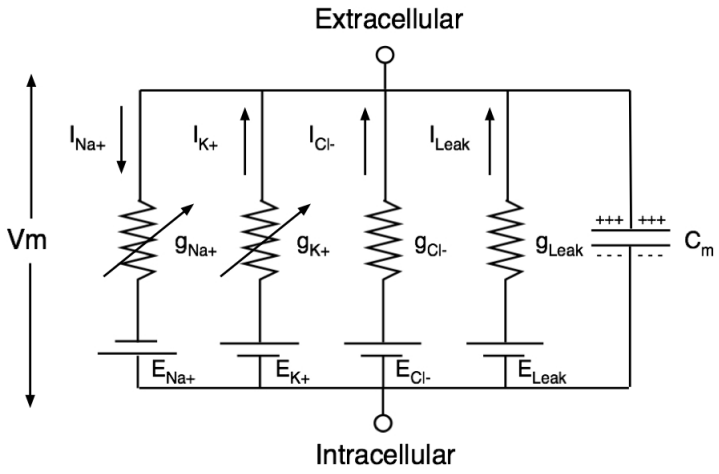

Figure 1.3: Example of an equivalent circuit model for a neuron membrane [48].

1.3 The Retina

The retina, found in most vertebrates, is a thin (0.5 mm) film of tissue in the outer layers of the eye, as shown in Figure 1.4. Despite its physiological location, the retina is considered to be an extension of the brain. The purpose of the retina is to convert incoming light stimuli into electrical information that can be interpreted by the brain and transformed into visual images; a process known as phototransduction. The retina tissue is organized into ten layers, each composed of various types of neurons, as shown in Figure 1.5. The receptor neurons responsible for initializing phototransduction are called photoreceptors and come in two types: rods and cones, named after their respective anatomical shapes. In humans, photoreceptors make up about 70% of all receptor neurons, a testament to how important vision is to our nervous systems. Rods and cones each have different functions and their relative abundance in a given species depends primarily on how active the species is during the day or night. For instance, rods are more sensitive to light than cones and are responsible for night vision so they are usually more abundant in nocturnal species. On the other hand, cones are more active in daylight since they respond primarily to high-intensity light. Cones are also responsible for interpreting color.

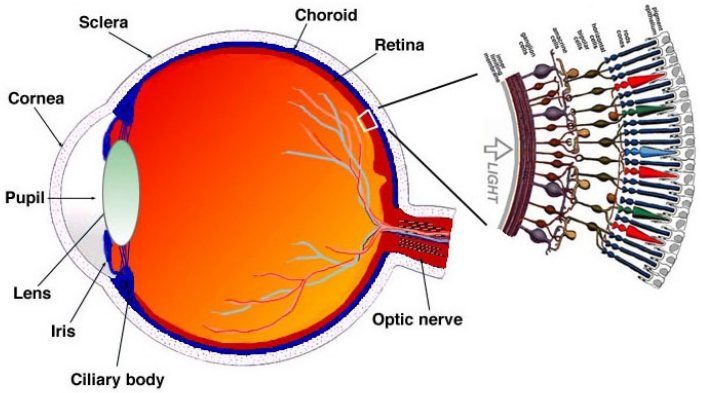

Figure 1.4: Simple diagram of a human eye [29].

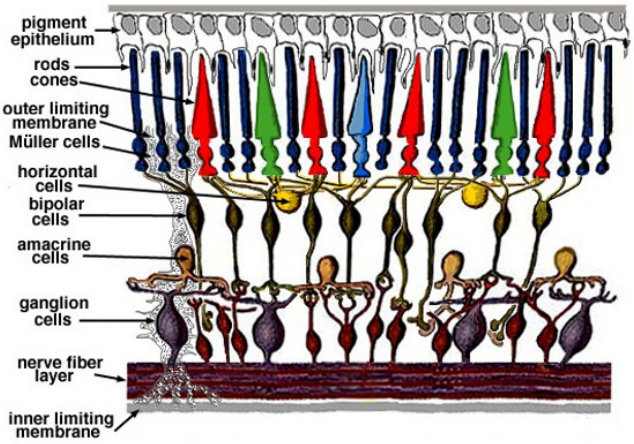

Figure 1.5: A magnified view of the layers of the retina [29].

The Outer Plexiform Layer

The layer of the retina that is of concern to us in this study is the outer plexiform layer (OPL). In this layer, the synaptic terminals of rods and cones form synapses with two other types of neurons: horizontal cells (HCs) and bipolar cells (BCs). The bipolar cells carry visual information to the inner plexiform layer and the horizontal cells form a network connected through gap junctions which is confined to the OPL. Horizontal cells act as communication buffers between photoreceptors and bipolar cells via complex feedback mechanisms. Photoreceptors translate

visual information into electrical information through changes in their membrane potentials. Horizontal cells in turn respond to these changes, providing the input to bipolar cells. Throughout the rest of this paper, we will consider a particular type of synapse in the OPL formed by a cone, a horizontal cell and a bipolar cell, referred to as a triad synapse.

The Triad Synapse

The synaptic terminal of a cone, called the cone pedicle, forms a cavity-like structure with a highly convoluted geometry. The pedicle is invaginated by multiple spines extending from the dendrites of horizontal cells and bipolar cells. A triad synapse is a synapse in which a bipolar cell, flanked by two or more horizontal cells, comes into close proximity with the cone pedicle. In a typical goldfish cone pedicle, there are on average 5-16 triad synapses [24]. An idealized diagram of a two dimensional slice of a triad synapse is shown in Figure 1.6.

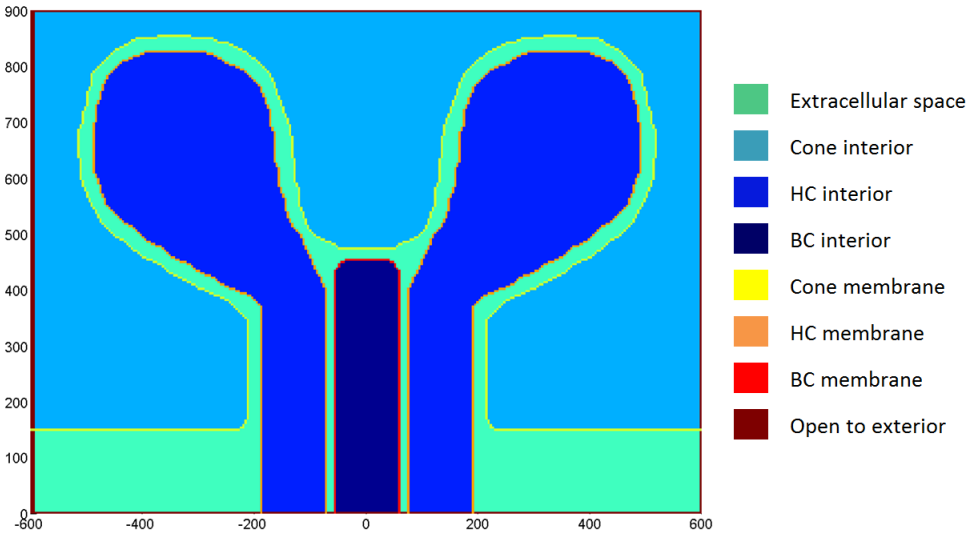

Figure 1.6: A color-coded diagram of the triad synapse. Length scale is in nanometers.

Neurotransmission in the triad synapse is modulated by the flow of calcium ions through the cone pedicle membrane. The area inside the cone pedicle directly across from the bipolar cell contains vesicles that release the neurotransmitter glutamate. The rate at which glutamate is being released from the cone is proportional to the cone's interior calcium levels.

The particular experiment that we apply our model to was performed by Verweij et al. in [45] on goldfish retinas. In their experimental setup, an isolated goldfish retina is saturated with a 65 μm bright spot of red light. The calcium current through the cone membrane is then measured with and without background illumination using patch clamp techniques with a Ringer's solution designed to block the currents contributed by other ions. Figure 1.7 shows a schematic demonstrating this setup. See [45] for a complete description of this experiment.

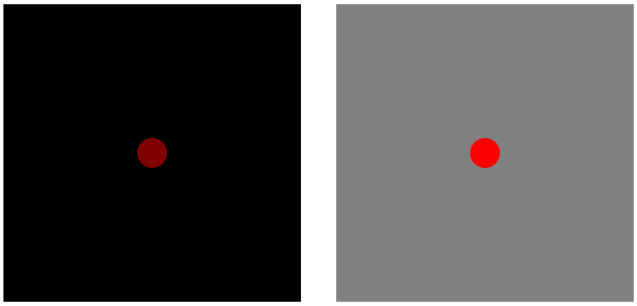

Figure 1.7: A schematic to demonstrate the goldfish experiments. *Left*: A retina saturated with a bright spot without background illumination. *Right*: A retina saturated with a bright spot plus background illumination.

In the absence of background illumination, cones depolarize which activates voltage-gated calcium channels in the cone, increasing the cone's interior calcium levels. This in turn triggers the cone membrane to release more glutamate, which diffuses across the synaptic cleft and binds to receptor sites on the horizontal cell. The binding of glutamate activates cation-specific channels in the horizontal cell, allowing positive charge to flow in, resulting in depolarization of the postsynaptic membrane. On the other hand, when the background is illuminated, cones hyperpolarize, leading to a reduction in glutamate release, which causes less glutamate-gated channels in the horizontal cell to open and therefore less positive charge enters the horizontal cell, leading to a hyperpolarization of the horizontal cell membrane.

It has been observed that when horizontal cells become hyperpolarized the net result is an increase in cone interior calcium levels, which then increases glutamate release and brings the horizontal cell back to its resting state. This suggests a negative feedback pathway from horizontal cells to cones. The existence of this feedback pathway is irrefutable although the

underlying mechanism responsible for it has been a subject of heated debate for over twenty years. In the next section, we discuss three hypotheses that have been proposed over the years to explain this feedback mechanism.

1.4 Three Competing Hypotheses

We will now explore the three currently existing hypotheses regarding the feedback mechanisms described in the last section: the ephaptic hypothesis, the pH hypothesis and the GABA hypothesis. Although this thesis is focused only on testing the ephaptic hypothesis, it is of interest to review all three hypotheses to get a better understanding of the biological complexity of the problem. Experimental evidence exists throughout the literature that both supports and contradicts these three hypotheses, making it difficult to draw any significant conclusions. The most recent research in this area suggests that the ephaptic and pH effects are both present but operate on different time scales. The GABA hypothesis has also had some experimental support although it is currently believed to be the weakest of the three. A reasonable, but somewhat unsatisfying explanation is that all three proposed mechanisms play a role that varies significantly between different species and types of horizontal cells.

The Ephaptic Hypothesis

The ephaptic hypothesis was first proposed in 1986 by Byzov and colleagues [7] and has since been repeatedly tested and modified. In short, the ephaptic hypothesis claims that the negative feedback pathway from horizontal cells to cones is electrical in nature and thus is governed by the electric potential. The specialized geometry of the triad synapse contains narrow extracellular regions between horizontal cells and the cone pedicle which have a relatively large resistivity. When ionic current passes from these high-resistance regions into the horizontal cell, via ion channels, this causes a potential drop in the extracellular cleft, i.e., the potential in the cleft becomes more negative. The cone membrane senses this potential drop in the cleft as a depolarization, which in turn activates calcium channels to open. When the horizontal cell becomes

hyperpolarized under background illumination, its channels will then draw in more current from the extracellular cleft, enhancing the cone membrane depolarization, which ultimately leads to an increase in interior calcium levels in the cone. In a voltage-clamp experiment, this increase in cone calcium levels under background illumination is seen as a shift in the current-voltage curve to more negative potentials.

In order for this hypothesis to work, there must be active channels in the horizontal cell to draw in current. Byzov originally proposed the glutamate-gated channels at the tips of the horizontal cell as the candidate [7]. However, this idea was discarded when Kamermans and colleagues put it to the test on goldfish [27]. In their experiments, they used dinitroquinoxaline (DNQX), a glutamate antagonist, to block the transmembrane current through the glutamate-gated channels. Their results indicated that this did not affect the shift in the current-voltage curves. Instead of abandoning the hypothesis completely, they instead modified it by proposing that hemichannels in the tips of the horizontal cells were responsible for the inward current. Hemichannels are often considered as one-way gap junctions, in the sense that they connect the interior of a cell to the extracellular space and do not have a gating mechanism, i.e., they constantly remain open. This idea was driven by physiological studies that confirmed that such channels are indeed located on the horizontal cell and are in close proximity with the calcium channels and glutamate release sites [22]. The modified hypothesis has gained momentum in recent years due to the successful experiments designed to test it. In one creative experiment, Kamermans and colleagues performed identical voltage clamp experiments on two groups of zebrafish: a genetically modified group that lacked the codons necessary to specify the hemichannel proteins and an unmodified control group [28]. The results showed that the current-voltage curves in the modified subjects did not get shifted, whereas the curves for the control group were shifted, a clear indication that the feedback is indeed dependent on hemichannels.

Although the ephaptic hypothesis has enjoyed some experimental success, it has its problems as well. A circuit model proposed by Dmitriev et al. concludes that the resistance of the extracellular cleft must be extremely large to induce the observed feedback and claim that

such an extreme resistance value is not physically reasonable [12]. In addition, the other two hypotheses have received some experimental support.

The pH Hypothesis

The pH hypothesis proposes that feedback is modulated by changes in extracellular proton concentrations. According to the hypothesis, hyperpolarization of horizontal cells alkalinizes the extracellular space which serves to alter the gating mechanism of pH-sensitive calcium channels in the cone membrane [5, 21]. However, the mechanism by which horizontal cell polarization controls extracellular pH levels is still unknown, although researchers have proposed many possible candidates. See [24, 46, 6, 21] for more details about the proposed mechanisms.

The pH hypothesis has a fair amount of experimental support. It has been shown that extracellular pH levels can affect voltage-sensitive calcium channels [11, 41]. Further, experiments with goldfish, tiger salamanders and macaque monkeys have shown that inhibition of extracellular pH fluctuations, induced by inserting high concentrations of artificial pH buffers, can greatly affect the feedback responses [2, 8, 10, 21, 46].

The validity of this hypothesis has also been questioned. One study in the goldfish retina showed that feedback responses were not altered in the presence of high concentration of HEPES, an artificial pH buffer [32, 24]. It has also been argued that the experimental techniques used to test the hypothesis can have unintended side effects that would affect other feedback mechanisms [15]. For example, the insertion of pH buffers can cause acidification of the intracellular horizontal cell solution, which can inhibit hemichannel activity.

The GABA Hypothesis

The GABA hypothesis asserts that feedback is modulated by a chemical neurotransmitter with γ-aminobutyric acid (GABA) being the primary candidate [13, 18, 38, 40]. The theory claims that horizontal cells constantly release GABA which diffuses across the extracellular space, binding to the cone membrane, inhibiting calcium channels. Under background illumination

induced hyperpolarization of the horizontal cell, the quantity of GABA released by the horizontal cell is reduced, allowing more calcium to flow into the cone.

The GABA hypothesis has received some experimental support. A GABA-synthesizing enzyme, known as glutamic acid decarboxylase (GAD), has been found to exist in some horizontal cells of certain animals [9, 19, 23, 31, 44]. It has also been observed that GABA release sites on horizontal cells act in a manner consistent with the hypothesis, i.e., they are inhibited by hyperpolarization [1, 33, 42, 43]. Most importantly, several pharmacological studies of the catfish and carp retina have revealed that application of GABA antagonists does indeed affect feedback under background illumination [30, 36, 37].

Most opposition to the GABA hypothesis stems from the fact that Kamermans' experiments were able to alter feedback responses in a GABA-independent manner. It is most likely that GABA does play some role in the overall process but only in certain instances and for certain species. However, it is still unclear as to whether or not the feedback is dominated by a GABA-ergic mechanism.

Chapter 2

THE MATHEMATICAL MODEL

2.1 Drift-Diffusion Equations

Consider a region such as that shown in the two dimensional slice of the triad synapse in Figure 1.6. This region can be separated into four compartments: cone interior, HC interior, BC interior and extracellular. Each compartment is assumed to be filled with water and the four common biological ions Ca^{2+}, Na^{+}, K^{+} and Cl^{-}, which we treat as continuous charge, rather than individual ions. This continuum model has been applied successfully in many applications [14, 39, 17, 16].

The presence of dissociated ions in a salt bath induces a potential field, which in turn affects the flow of ions. Our goal is then to model the evolution of the particle densities (particles per volume) of each ionic species and the electric potential. To do so, we introduce a system of partial differential equations, known as the drift-diffusion or Poisson-Nernst-Planck equations, that hold in the various compartments. Treatment of the state variables on the membranes and boundaries will be discussed in later sections of this chapter.

To introduce the drift-diffusion model, let $\mathbf{x}$ denote any point in the domain shown in Figure 1.6 that is not on a membrane or outer boundary and let t denote time. Define $n_i(\mathbf{x},t)$ to be the particle density of the ith ionic species at the point $\mathbf{x}$ at time t where $i \in \{ Ca^{2+}, Na^{+}, K^{+}, Cl^{-}\}$. Likewise, define $\phi(\mathbf{x},t)$ to be the electric potential at the point $\mathbf{x}$ and time t. By requiring conservation of charge for each ionic species, we obtain the continuity equation

$$\frac{\partial n_i}{\partial t} + \nabla \cdot \mathbf{f}_i = 0, \quad i \in \{Ca^{2+}, Na^{+}, K^{+}, Cl^{-}\} \tag{2.1}$$

where $\mathbf{f}_i$ is the particle flux of the ith ionic species. Gauss's Law relates the particle densities to the electric potential:

$$\nabla \cdot (\varepsilon \nabla \phi) = -\rho, \tag{2.2}$$

where ε is the dielectric coefficient of water and ρ is the total charge density. To obtain ρ we

sum over all charge contributions from the ions plus any immobile "background" charge

$$\rho = \rho_0 + \sum_i q_i n_i \tag{2.3}$$

where ρ_0 is the background charge density and q_i is the ionic charge of species i. For our problem, we do not resolve the detailed channel structure within the membranes so we take $\rho_0 \equiv 0$. We now turn to choosing an expression for $\mathbf{f}_i$, which is where the modeling comes in. Like any chemical species, ions are subject to diffusion and the diffusive flux follows Fick's Law:

$$\mathbf{f}_{i,\text{diffusion}} = -D_i \nabla n_i \tag{2.4}$$

where D_i is the diffusion coefficient of ionic species i. The diffusion coefficient is determined experimentally and is dependent upon the medium in which the ions flow and the physical properties of the ion. In addition, ions also respond to the electric field, causing the drift flux derived from the microscopic version of Ohm's Law:

$$\mathbf{f}_{i,\text{drift}} = z_i \mu_i n_i \mathbf{E}, \quad \mathbf{E} = -\nabla \phi \tag{2.5}$$

where μ_i is the mobility coefficient of ionic species i. The diffusion and mobility coefficients satisfy the Einstein relation $D_i = \mu_i k_B T / e$ where k_B is the Boltzmann constant, T is the absolute temperature of the medium and e is the unit charge. For most biological applications, $T \approx$ 310 K, a typical body temperature, so $k_B T \approx 1/40$ eV. Combining the two forms of flux from equations 2.4 and 2.5, we get the total particle flux for the drift-diffusion model:

$$\mathbf{f}_i = z_i \mu_i n_i \mathbf{E} - D_i \nabla n_i. \tag{2.6}$$

The particle flux $\mathbf{f}_i$ for each ionic species can be converted into electric current densities $\mathbf{j}_i$ via the simple relation

$$\mathbf{j}_i = q_i \mathbf{f}_i \tag{2.7}$$

and the total current density $\mathbf{j}$ is

$$\mathbf{j} = \sum_i \mathbf{j}_i. \tag{2.8}$$

Parameter	Value	Units	Description
D_{Ca}	0.8	nm^2/ns	diffusion coefficient of Ca^{2+}
D_{Cl}	2	nm^2/ns	diffusion coefficient of Cl^-
D_{Na}	1.3	nm^2/ns	diffusion coefficient of Na^+
D_K	2	nm^2/ns	diffusion coefficient of K^+
μ_{Ca}	32	$nm^2/(V \cdot ns)$	mobility coefficient of Ca^{2+}
μ_{Cl}	80	$nm^2/(V \cdot ns)$	mobility coefficient of Cl^-
μ_{Na}	52	$nm^2/(V \cdot ns)$	mobility coefficient of Na^+
μ_K	80	$nm^2/(V \cdot ns)$	mobility coefficient of K^+
ε	80	none	dielectric coefficient of water

Table 2.1: Physical parameters used in drift-diffusion equations.

In general, the parameters D_i, μ_i, ε and ρ_0 can be treated as function of space. For our purposes, it is reasonable to assume that these parameters are constant in the physical domain of the problem since we do not model the detailed spatial structure of the channels within the membranes nor do any of the compartments differ in any significant way. The constant values used for the parameters are shown in Table 2.1. To summarize, the drift-diffusion model for our particular problem reduces to the system

$$\frac{\partial n_i}{\partial t} = D_i \nabla^2 n_i + z_i \mu_i \nabla \cdot (n \nabla \phi) \tag{2.9}$$

$$\nabla^2 \phi = -\frac{1}{\varepsilon} \sum_i q_i n_i \tag{2.10}$$

$$i \in \{Ca^{2+},\ Na^+,\ K^+,\ Cl^-\}$$

which we will make frequent reference to throughout this paper. This model forms a nonlinear parabolic/elliptic system of $N_{species} + 1$ partial differential equations where $N_{species}$ is the number of ionic species included in the model. The state variables of the model are n_i and ϕ, which have Dirichlet and/or Neumann boundary conditions.

2.2 Bath Densities

It is known experimentally that the ion densities in biological fluids remain at constant values when far away from cell membranes. The values of these constant ion densities are referred to as the bath densities, denoted by $n_{b,i}$ and have been measured for several cases. However,

Ion	Intracellular	Extracellular	Units
Ca^{2+}	10^{-4}	2	mM
Cl^{-}	160	146.5	mM
Na^{+}	10	140	mM
K^{+}	150	2.5	mM

Table 2.2: Values of the intracellular and extracellular bath densities for the four common biological ions used in simulations.

for any given ionic species, the bath densities can be very different depending on whether the region is inside a cell or outside a cell. For example, the typical intracellular bath density for calcium in a mammalian organism is $n_{b,Ca} = 10^{-4}$ mM whereas the extracellular bath density is $n_{b,Ca} = 2$ mM. It is also known that biological fluids maintain charge neutrality away from membranes. To ensure this, we must enforce the condition

$$\sum_i q_i n_{b,i} = 0. \tag{2.11}$$

However, the experimentally measured values of the four common ionic species do not generally satisfy this relation since there are a number of other charged molecules that contribute. To get around this, we use the typical bath densities for the positive ions and treat chloride as the general negative charge carrier, setting

$$n_{b,Cl} = \sum_{i \neq Cl} z_i n_{b,i}. \tag{2.12}$$

Since we are most interested in studying steady state solutions, the choice of initial conditions is somewhat arbitrary, as long as we begin with a charge neutral domain. We use the most obvious choice, which is

$$n_i(\mathbf{x}, 0) = n_{b,i}, \tag{2.13}$$

i.e., all ions begin with uniform densities with their intracellular or extracellular bath values. The values we use for the bath densities are shown in Table 2.2. Note that the values for $n_{b,Cl}$ are not typical and have been adjusted to ensure charge neutrality.

2.3 Membrane Surface Charge Densities

As mentioned in the previous section, biological fluids maintain charge neutrality away from membranes. However, as we will see in this section, charge layers can accumulate on membranes, violating the local neutrality. To demonstrate this, we must develop a model for the membrane surface charge densities. Our approach to modeling the membrane follows that of Mori et al. in [34, 35]. However, in their treatment, they use asymptotic expansions with intermediate matching to avoid dealing with charge layers, whereas we actually resolve these layers.

The main idea is to treat the membrane as a double-valued sheet in 3D. We label the sides of the membranes as $+$ (intracellular) and $-$ (extracellular). The membrane is modeled as a capacitor with zero thickness in which ions can accumulate on and/or pass through either side, resulting in a surface charge density, denoted as $\sigma_i^{\pm}$, where i indexes the four ionic species and the $\pm$ superscript denotes the side of the membrane. The state variables of the drift-diffusion model, n_i and ϕ, are also defined on the membrane and are double-valued, denoted as $n_i^{\pm}$ and $\phi^{\pm}$, respectively. Charge conservation equations can be derived for $\sigma_i^{\pm}$, although we postpone this derivation to later in the section. To obtain the membrane boundary conditions for the ion densities, we will need to devise a method of relating the spatial charge densities $n_i^{\pm}$ to the surface charge densities $\sigma_i^{\pm}$.

Relating Surface Charge Densities to Particle Densities

Consider an arbitrary point p on a membrane and let x be the axis perpendicular to the membrane at p such that the origin is at p. Suppose the x axis is oriented such that $x > 0$ on the $+$ side of the membrane and $x < 0$ on the $-$ side. We then assume that all of the excess charge along both sides of the x axis accumulates on the $\pm$ sides of the membrane and we ignore contributions

from other directions. Making this 1D approximation along the x axis, we have

$$\sigma_i^{\pm} = \int_0^{\pm\infty} q_i(n_i^{\pm}(x) - n_{b,i}^{\pm})\, dx \tag{2.14}$$

where $q_i(n_i^{\pm}(x) - n_{b,i}^{\pm})$ represents the spatial density of the excess charge. To continue with this model, we must now have a way of approximating this integral.

With this 1D approximation and assuming thermal equilibrium in which no current flows, the ion densities must satisfy

$$n_i^{\pm}(x) = n_{b,i}^{\pm} \exp\left\{ -\frac{q_i[\phi^{\pm}(x) - \phi_b^{\pm}]}{k_B T} \right\} \tag{2.15}$$

where $\phi_b^{\pm}$ is the asymptotic potential away from the membrane and $\exp\left\{ -\frac{q_i[\phi^{\pm}(x) - \phi_b^{\pm}]}{k_B T} \right\}$ is the Boltzmann factor from the theory of thermal equilibrium. Inserting this into the 1D version of equation 2.10 yields the Poisson-Boltzmann equation

$$\frac{d^2\phi^{\pm}}{dx^2} = -\frac{1}{\varepsilon} \sum_i q_i n_{b,i}^{\pm} \exp\left\{ -\frac{q_i[\phi^{\pm}(x) - \phi_b^{\pm}]}{k_B T} \right\}. \tag{2.16}$$

Linearizing equation 2.16 and using the charge neutrality condition $\sum_i q_i n_{b,i}^{\pm} = 0$, we get the approximation

$$\frac{d^2\phi^{\pm}}{dx^2} \approx \frac{1}{\varepsilon k_B T} \left[\sum_i q_i^2 n_{b,i}^{\pm} \right] (\phi^{\pm}(x) - \phi_b^{\pm}) \tag{2.17}$$

for which the solution is

$$\phi^{\pm}(x) = \phi_b^{\pm} + [\phi^{\pm}(0) - \phi_b^{\pm}] e^{-|x|/l_D^{\pm}} \tag{2.18}$$

where

$$l_D^{\pm} = \sqrt{\frac{\varepsilon k_B T}{\sum_i q_i^2 n_{b,i}^{\pm}}} \tag{2.19}$$

is a parameter with units of length, referred to as the Debye length, which is typically around 1 nm for biological baths. Indeed, using the parameter values from Tables 2.1 and 2.2, we have that $l_D^{+} \approx 0.783613$ nm and $l_D^{-} \approx 0.787561$ nm. Note that in the solution given in 2.18, we neglect one of the fundamental solutions of 2.17 for each side of the membrane. This is done to ensure a physical solution in which $\phi^{\pm}(x)$ is bounded as $x \to \pm\infty$. Notice that the solution

is indicative of an exponentially decaying boundary layer near $x = 0$ (the membrane) with a thickness $l_D^{\pm}$. Inserting 2.18 into 2.15 and linearizing the result gives

$$n_i^{\pm}(x) = n_{b,i}^{\pm} \exp\left\{ -\frac{q_i[\phi^{\pm}(0) - \phi_b^{\pm}]e^{-|x|/l_D^{\pm}}}{k_B T} \right\} \approx n_{b,i}^{\pm} \left(1 - \frac{q_i[\phi^{\pm}(0) - \phi_b^{\pm}]e^{-|x|/l_D^{\pm}}}{k_B T} \right). \quad (2.20)$$

We can now approximate the integral from 2.21 as

$$\begin{aligned} \sigma_i^{\pm} = \int_0^{\pm\infty} q_i(n_i^{\pm}(x) - n_{b,i}^{\pm})\, dx &\approx -\frac{n_{b,i}^{\pm} q_i^2[\phi^{\pm}(0) - \phi_b^{\pm}]}{k_B T} \int_0^{\pm\infty} e^{-|x|/l_D^{\pm}}\, dx \\ &= -\frac{n_{b,i}^{\pm} q_i^2[\phi^{\pm}(0) - \phi_b^{\pm}] l_D^{\pm}}{k_B T}. \end{aligned} \quad (2.21)$$

Now using the fact that $n_i^{\pm}(0) \approx n_{b,i}^{\pm}\left(1 - \frac{q_i[\phi^{\pm}(0) - \phi_b^{\pm}]}{k_B T}\right)$, we get the relation

$$\sigma_i^{\pm} = q_i l_D^{\pm}(n_i^{\pm} - n_{b,i}^{\pm}). \quad (2.22)$$

Here we have replaced $n_i^{\pm}(0)$ with $n_i^{\pm}$, with the understanding that $n_i^{\pm}$ is the particle density on the membrane.

Note that the linearized approximations we use here are only good when

$$|q_i(\phi^{\pm}(x) - \phi_b^{\pm})/(k_B T)| \ll 1 \quad (2.23)$$

which is the case for this problem and most biological applications. In Appendix A, we give a description of how to relate the surface charge densities and particle densities when this inequality is violated.

Conservation Equation for Surface Charge Densities

We now use 2.22 to derive a conservation equation for the time evolution of $\sigma_i^{\pm}$. Taking the partial derivative with respect to t of each side of 2.22 gives

$$\frac{\partial \sigma_i^{\pm}}{\partial t} = \frac{\partial}{\partial t}\left[q_i l_D^{\pm}(n_i^{\pm} - n_{b,i}^{\pm}) \right] = q_i l_D^{\pm} \frac{\partial n_i^{\pm}}{\partial t}. \quad (2.24)$$

Assuming that the charge on the membrane is overall neutral, the particle densities on the membranes must satisfy equation 2.1. Using this fact and the definition of electric current density in 2.7, we have

$$\frac{\partial \sigma_i^{\pm}}{\partial t} = -l_D^{\pm} \nabla \cdot \mathbf{j}_i^{\pm} \quad (2.25)$$

which amounts to a decoupled system of ordinary differential equations in time, i.e., the evolution of each ionic species at each point are independent of each other. The initial conditions for $\sigma_i^{\pm}$ at each point are automatically determined by the initial conditions for the particle densities. Using equation 2.22, we have

$$\sigma_i^{\pm}(0) = q_i l_D^{\pm}(n_i^{\pm}(0) - n_{b,i}^{\pm}) = 0. \tag{2.26}$$

In the preceding derivation, there is an implicit assumption that no current flows through the membrane. In order to model ion channels in which charge can be exchanged across the membrane, we simply insert an extra term for the transmembrane current density on the RHS of 2.25 which results in

$$\frac{\partial \sigma_i^{\pm}}{\partial t} = -l_D^{\pm} \nabla \cdot \mathbf{j}_i^{\pm} \mp j_{m,i} \tag{2.27}$$

where $j_{m,i}$ is the transmembrane current. Note that we are using the typical sign convention for $j_{m,i}$ in which current flowing into a cell is negative and current flowing out of a cell is positive. Modeling the transmembrane current for different scenarios can itself be an enormous problem. Given the complexity of ion channels, there is practically no limit as to how detailed the model for $j_{m,i}$ can be. We will address how we model $j_{m,i}$ in the next section.

2.4 Transmembrane Current

For our problem, we model two types of channels in specific locations on the membranes. As discussed in the introduction, there are two main types of channels important to ephaptic feedback: voltage-gated calcium channels in the cone pedicle membrane and hemichannels in the horizontal cell membrane. Much research has gone into understanding the currents in these channels and there is plenty of good data available to make use of [26, 24].

Calcium Channels in the Cone Membrane

We model the membranes as a continuum of channels with a uniform density. The calcium channels in the cone have been experimentally shown to obey a nonlinear Ohm's law with a

voltage dependent conductance function [26], which we use in our model:

$$j_{m,Ca} = \frac{g_{Ca,CP}(V_m - E_{Ca,CP})}{N_s A_m[1 + \exp\{(\theta - V_m)/\lambda\}]} \tag{2.28}$$

where $V_m = \phi^+ - \phi^-$ is the membrane potential, $g_{Ca,CP}$ is the maximum calcium conductance, $E_{Ca,CP}$ is the reversal potential of calcium, N_s is the average number of calcium channel sites in a cone pedicle (twice the number of triad synapses), A_m is the surface area of the section of the cone pedicle containing calcium channels and θ and λ are curve fitting parameters. The normalization factors N_s and A_m require some explanation. Equation 2.28 is motivated by experimental data, which measures actual currents instead of current densities. Further, the experiments measure the total current through a given cone pedicle, which contains many triad synapses. On average, each pedicle has about $N_s = 20$ calcium channel sites. Also, the area of the region of the cone pedicle containing calcium channels, A_m, we estimate to be about 0.1 μm^2. Thus dividing the current by A_m converts it into a current density and dividing by N_s gives the average current density over a given channel site.

The formula for the calcium current in equation 2.28 has an interesting stochastic interpretation. In reality, a given calcium channel is either open, with conductance $g_{Ca,CP}$ or closed, with zero conductance. Suppose that the transmembrane potential at a given channel is V_m. We can interpret the state of the channel as a Bernoulli random variable with the two possible states of OPEN or CLOSED, with a parameter $p(V_m)$ that represents the probability that the channel is in the OPEN state. The expected value of the conductance is thus $g_{Ca,CP} \cdot p(V_m)$. Comparing this to equation 2.28, we see that

$$p(V_m) = \frac{1}{1 + \exp\{(\theta - V_m)/\lambda\}} \tag{2.29}$$

which is a sigmoidal shaped curve, often referred to in the literature as the activation curve, in which θ represents the membrane potential at which $p(\theta) = 1/2$. For this reason, θ is referred to as the half-activation potential. This interpretation is consistent with the fact that depolarization of cone membranes opens calcium channels since $p \to 0$ as $V_m \to -\infty$ and $p \to 1$ as $V_m \to +\infty$.

Parameter	Value	Units	Description
E_{Ca}	50	mV	reversal potential of Ca^{2+}
E_{Na}	50	mV	reversal potential of Na^{+}
E_K	-60	mV	reversal potential of K^{+}
g_{Ca}	1.5	nS	conductance of Ca^{2+} current
g_{Na}	1.5	nS	conductance of Na^{+} current
g_K	2.5	nS	conductance of K^{+} current
g_{hemi}	5.5	nS	total hemichannel conductance
C_m	1	μF/cm^2	capacitance per area
A_m	0.1	μm^2	HC spine head area
N_s	20	none	number of HC spines per synapse

Table 2.3: Hemichannel and other membrane parameters based on experimental estimations.

Hemichannels in the Horizontal Cell Membrane

The hemichannels in the horizontal cell are believed to be non-specific cation channels [24] and thus we allow all cations to pass through them. The current-voltage relationship for hemichannels is experimentally observed to be linear, with an overall reversal potential of zero and a constant conductance of g_{hemi} [28]. However, this includes the current from all cations and does not give any information about individual ionic currents. A reasonable approach is then to model each current density with a linear Ohm's law:

$$j_{m,i} = g_i(V_m - E_i)/(N_s A_m). \tag{2.30}$$

and impose the constraints

$$\sum_i g_i = g_{hemi} \tag{2.31}$$

and

$$\sum_i g_i E_i = 0 \tag{2.32}$$

to guarantee consistency with the experimental data. The hemichannel parameters are shown in Table 2.3. Note that the parameters for the cone are omitted from this table since we vary them for different simulations, which are discussed later.

Physical Location of Channels

The location of the calcium channels in the cone membrane and the hemichannels on the horizontal cell membrane are not arbitrary and in fact are located in such a way as to enable ephaptic communication. Figure 2.1 shows the regions in which experimentalists believe the channels are located [24], which we also use in our model. In order to be able to compare our results to experiment, we must approximate the current though an entire cone pedicle. To do this, we first compute the average current density over the channel region via the trapezoid rule for numerical integration and then multiply the result by the normalization factors N_s and A_m. Thus the calcium current for an entire cone pedicle, I_{Ca}, is approximated as

$$I_{Ca} = \frac{N_s A_m}{\ell_C} \int_C j_{m,Ca}\, ds \tag{2.33}$$

where C is the segment of the membrane containing the calcium channels and ℓ_C is the arc length of C.

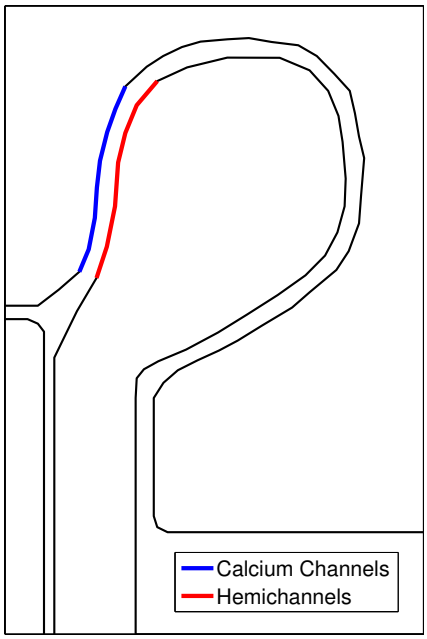

Figure 2.1: Physical locations of channels in triad synapse.

2.5 Membrane Boundary Conditions

Now we are ready to give the boundary conditions for the state variables on the membrane. Assuming we have solved equation 2.27 at the given time, we can use equation 2.22 to get the boundary conditions for $n_i^{\pm}$. Solving for $n_i^{\pm}$ gives

$$n_i^{\pm} = n_{b,i}^{\pm} + \frac{\sigma_i^{\pm}}{q_i l_D^{\pm}}. \tag{2.34}$$

One of the boundary conditions for ϕ on the membranes can be determined by treating the membrane as a capacitor with a surface charge density σ and capacitance per unit area C_m, resulting in the jump condition

$$[\phi] \equiv \phi^+ - \phi^- = \frac{\sigma}{C_m} \tag{2.35}$$

where σ is defined as

$$\sigma = \sum_i \sigma_i^+ = -\sum_i \sigma_i^-. \tag{2.36}$$

Note that this definition assumes the membrane remains charge neutral, i.e., any charge that accumulates on one side must be balanced by charge on the opposite side. This requirement implicitly gives us a second jump condition. Since we are assuming charge neutrality over the membrane, we have

$$[\mathbf{n}_m \cdot \nabla\phi] \equiv \mathbf{n}_m \cdot \nabla\phi^+ - \mathbf{n}_m \cdot \nabla\phi^- = 0 \tag{2.37}$$

where $\mathbf{n}_m$ is the unit normal vector of the membrane pointing from the $-$ side to the $+$ side. In other words, the normal component of the electric field is continuous across the membrane. Note that the values of the ion densities on each side of the membrane are computed independently of the other side. However, upon spatial discretization, equations (2.35) and (2.37) form a linear system of equations for ϕ^+ and ϕ^-, which couples the intracellular and extracellular solutions. We will discuss how equation 2.37 can be used to derive a linear algebraic relation between ϕ^+ and ϕ^- in the subsequent chapter on numerical methods.

2.6 Outer Boundary Conditions

A problem of this nature has both interior and exterior boundaries. The interior boundaries are the membranes, which have boundary conditions discussed in the preceding section. The exterior boundaries are formed by the rectangle enclosing the region and do not have precise boundary conditions in the physical sense. We use a mixture of Dirichlet and Neumann boundary conditions on the outer boundary, driven by physical intuition. Since we apply the model to two different computational grids, we postpone presenting the exact outer boundary conditions until the grids are discussed in the next chapter. Instead, we give a general description of the possible types of boundary conditions. The most natural boundary condition to use for the particle densities is the Dirichlet condition

$$n_i = n_{b,i} \tag{2.38}$$

since it is reasonable to assume the particle densities remain at their bath values away from membranes. Along any axis of symmetry, such as $x = 0$ in the region shown in Figure 1.6, we use the homogeneous Neumann boundary condition

$$\mathbf{n} \cdot \nabla n_i = 0 \tag{2.39}$$

where $\mathbf{n}$ is the outward pointing unit normal vector to the boundary. The boundary conditions for ϕ are chosen in a way that attempts to mimic a voltage clamp experiment. In such an experiment, micro electrodes that are held at fixed potentials are inserted at specific locations, usually one inside a cell and the other "ground" electrode far away from the cell. Along certain boundaries, it is then appropriate to use the Dirichlet boundary condition

$$\phi = V_{clamp} \tag{2.40}$$

where V_{clamp} is the clamped potential, or holding potential, with respect to ground. Along other boundaries, a natural condition for the potential is the homogeneous Neumann condition

$$\mathbf{n} \cdot \nabla \phi = 0. \tag{2.41}$$

Chapter 3

NUMERICAL METHODS

In this chapter, we give a detailed account of the numerical methods used in the simulations. In particular, we discuss the spatiotemporal discretization of the drift-diffusion equations and boundary conditions along with the methods used to solve the discretized systems of equations. During the first phase of this research, we focused on modeling a strip of the extracellular space between a cone cell and horizontal cell using a simple rectangular domain. Later, we developed the code to do simulations on a more general grid with complex geometry and interior membranes. Although most of the numerical methods used in these problems are fairly general and apply to both cases, we will at times need to discuss the details of the two problems separately.

3.1 Spatial Domains & Grids

In this section, we describe the spatial domains and computational grids used in simulations. Since the outer boundary conditions depend on the domain, it is appropriate to address them here as well.

Rectangular Grid

For the rectangular problem, we define the spatial domain $\Omega = [0,400] \times [0,40]$ where length units are in nanometers. The cone membrane is located along the top boundary ($y = 40$) and side boundaries ($x = 0,\ x = 400$). The horizontal cell membrane is located along $y = 0$ for $x \in [x_1, x_2]$ where x_1 and x_2 are varied for different simulations. The segments of the outer boundary that are not membranes are treated as being open to an exterior salt bath. This region is shown in Figure 3.1 for $x_1 = 10$, $x_2 = 380$.

The solution is computed on an $(M+1) \times (N+1)$ rectangular grid of points $(x_j, y_i) \in \Omega$

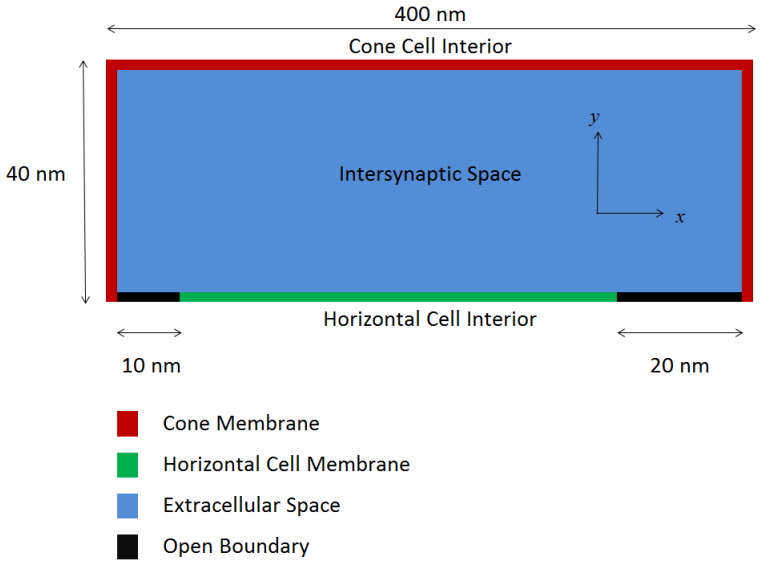

Figure 3.1: A diagram of the rectangular computational domain. Lengths are not to scale.

with

$$x_j = j\Delta x,\ j = 0,1,...,N,$$

$$y_i = i\Delta y,\ i = 0,1,...,M.$$

We use a uniform spacing in each direction, i.e., $\Delta x = 400/N$ and $\Delta y = 40/M$.

Although our model was formulated for a general problem containing intracellular and extracellular compartments separated by interior membrane boundaries, this particular application only simulates activity in the extracellular space. All the membrane boundary conditions are still used, they are just one-sided. This type of grid makes for a considerably easier problem to implement since the membrane boundaries are part of the outer boundary for the entire grid. In the next section, we will explore the complications of including interior boundaries.

Since we only simulate in the extracellular space for this problem, the model for the membrane surface charge densities reduces to

$$\frac{\partial \sigma^-}{\partial t} = \mathbf{n}\cdot\mathbf{j_i^-} + j_{m,i},\quad \sigma = \sum_i \sigma_i^-. \tag{3.1}$$

The calcium channels are modeled along the top segment of the cone membrane boundary and we use equation 2.28 to compute the transmembrane current density. Hemichannels are located

all along the horizontal cell membrane boundary with transmembrane current densities given by equation 2.30. The boundary conditions on the membranes in this case simplify to

$$n_i^- = n_{b,i}^- + \frac{\sigma_i^-}{q_i l_D^-}, \;\; \phi_{CP,HC}^- = \phi_{CP,HC}^+ - \frac{\sigma}{C_m} \tag{3.2}$$

where $\phi_{CP,HC}^+$ are specified constant values. The boundary conditions used for the openings (shown in black in Figure 3.1) are

$$n_i = n_{b,i}, \;\; \mathbf{n} \cdot \nabla \phi = 0. \tag{3.3}$$

Full Synapse Grid

We now consider the region shown in Figure 1.6 for the full synapse geometry. Since this region is symmetric about $x = 0$, we take the computational domain to be the right half only, as shown in Figure 3.2. In this case, the spatial domain is $\Omega = [0,600] \times [0,900]$. Just as in the rectangular case, the solution is computed on an $(M+1) \times (N+1)$ rectangular grid of points $(x_j, y_i) \in \Omega$ with

$$x_j = j\Delta x, \;\; j = 0,1,...,N,$$
$$y_i = i\Delta y, \;\; i = 0,1,...,M.$$

We use a uniform spacing in each direction, i.e., $\Delta x = 600/N$ and $\Delta y = 900/M$. However, in this problem, there are both intracellular and extracellular points. Further, the membrane points are located in the interior of the grid.

To define the membrane curves, we start with a free-hand drawing or digital picture of the region and load it into MATLAB as an image file. Using the *ginput* function from the MATLAB library, the user can manually select data points along the interior curves with the mouse and save the (x,y) coordinates. Assume n points are selected and define the sequence $(p_k)_{k=1}^n$ with $p_k = (x_k, y_k)$. The points in (p_k) are then moved to the nearest grid points under the Euclidean norm, i.e., $p_k \to (x_{J(k)}, y_{I(k)})$ where $(I(k), J(k)) = \min_{i,j}[(x_k - x_j)^2 + (y_k - y_i)^2]$. Now the boundary curve is a sequence of $n-1$ line segments that connect grid points. However,

in order to use a general finite volume method, we need to define the curve as a sequence of vertical, horizontal and diagonal lines that connect *adjacent* grid points, a process known as "meshing" the curve.

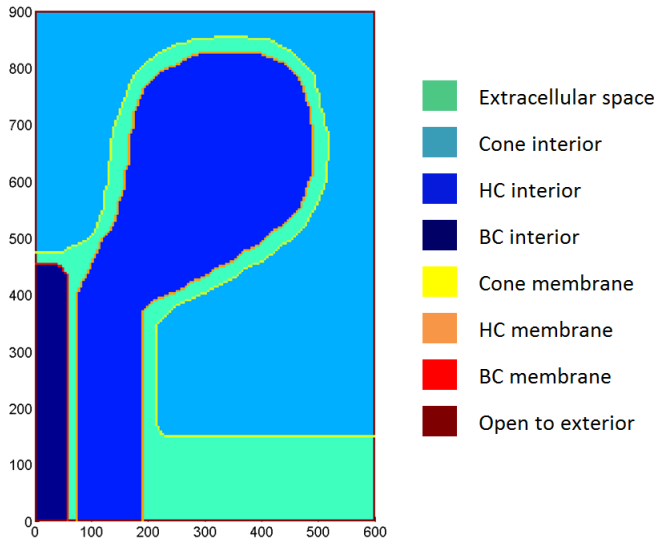

Figure 3.2: A color-coded diagram of the triad synapse. Length scale is in nanometers.

The algorithm for meshing a curve can be described by just considering how to connect any two points (say p_1 and p_2). Define the new sequence for the meshed curve as (r_k). Starting at any point, there are eight possible choices for the next point since there are eight neighboring grid points. Each of these eight directions has a corresponding unit vector $e_1, \ldots, e_8$. The algorithm for generating the sequence of points for the meshed curve is described below.

1. Set $q = p_1$
2. Add q to the sequence (r_k)
3. Set $u = (p_2 - q)/\|p_2 - q\|$
4. Compute $a_i = u \cdot e_i$ for $i = 1, 2, \ldots, 8$
5. Set $i^* = \arg\max_i a_i$
6. Set $q = q_{new}$ where q_{new} is the next point in the direction i^*
7. Go to step 2 and repeat until $q = p_2$

This process is then repeated to connect p_2 to p_3, etc. The last thing needed to define the grid is a labeling matrix that defines which points are of which type. In our problem, there are eight different types of points, so we can use the labels $1, 2, ..., 8$. The membrane boundary points have already been determined by the meshed curve but the labels for the interior points must be known as well. The boundary of each cell can be represented as a closed polygon and therefore we can use one of the standard algorithms for determining whether a point is inside or outside a polygon. The points that are found to be outside all cells are the extracellular points. The schematic shown in Figure 3.2 is actually the color plot of the labeling matrix for our region.

We now turn to the problem of defining the outer boundary conditions for this region. For the ion densities, we use the Dirichlet boundary condition from equation 2.38 everywhere, except along $x = 0$, which is considered an axis of symmetry. Along this axis, we use the homogeneous Neumann condition from 2.39. There are a total of four segments of the outer boundary where we use Dirichlet boundary conditions for the potential: one segment for each cell plus a segment designated to be used as a common reference potential. Figure 3.3 illustrates where the different boundary conditions are used. We can state these boundary conditions compactly as

$$\phi(x,y) = \begin{cases} U_{CP} & \text{if } y = 900, \\ U_{HC} & \text{if } (x,y) \in \{(x,y) \mid y = 0 \text{ and } (x,y) \text{ in HC } \}, \\ U_{BC} & \text{if } (x,y) \in \{(x,y) \mid y = 0 \text{ and } (x,y) \text{ in BC } \}, \\ U_{ref} & \text{if } y = 0 \text{ and } 500 \leq x \leq 600. \end{cases} \tag{3.4}$$

The remaining segments use the homogeneous Neumann boundary conditions from equation 2.41. The values for U_{CP}, U_{HC} and U_{BC} are the holding potentials discussed earlier. Note that the ground potential is not zero. This is because in a real experiment, the ground electrode would be very far from the computational region, which is why we use a general reference potential in the bottom right corner, instead of treating it as the absolute ground. The

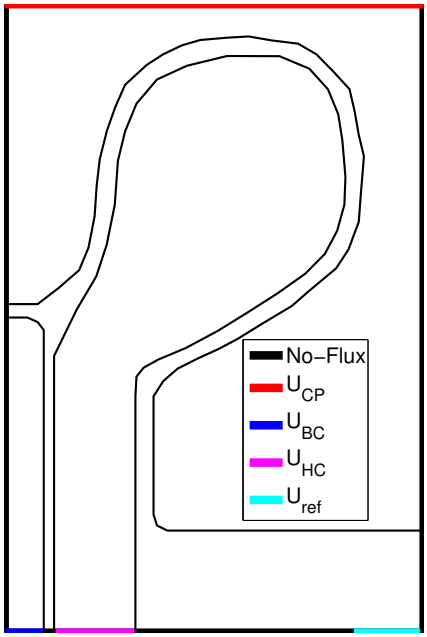

Figure 3.3: A diagram illustrating the outer boundary conditions of the domain for the potential.

holding potentials are chosen in different ways to simulate different cases. However, we always use the reference potential $U_{ref} = -40$ mV. There is nothing special about this value and it was chosen to coincide with the typical horizontal cell membrane potential so as not to create a large potential difference. This reference potential is necessary to ensure that the potentials for different simulations are measured with respect to the same ground.

3.2 Spatial Discretization: The Box Method

In this section, we discuss the techniques used to discretize all equations in space. All spatial derivatives are approximated using the second-order finite volume box method, which is a conservative scheme by construction. The box method can be visualized by placing a rectangle with horizontal side length Δx and vertical side length Δy around each grid point as shown in Figure 3.4. With this scheme, all state variables are defined at grid points and the flux is defined at midpoints of the box edges, shown as open circles in Figure 3.4. Note that this method was used for both the rectangular and complex grids, although in the rectangular case, it is equivalent to using second-order finite differences on a centered stencil. For notational purposes,

we will consider equation 2.9 for an arbitrary ionic species n and will thus omit the subscript denoting the ionic species. Let $n_{i,j}$ denote the numerical approximation of n at the point (x_j, y_i). We will also use the notation $\mathbf{f} = (f^1, f^2)$ for the components of the flux.

Discretization of the Drift-Diffusion Equations

We begin by considering the general conservation law that we wish to discretize

$$\frac{\partial n}{\partial t} = -\nabla \cdot \mathbf{f} \tag{3.5}$$

at an arbitrary interior grid point (x_j, y_i) that is not on the membrane. Let $B_{i,j}$ denote the box surrounding grid point (x_j, y_i). Integrating each side of 3.5 over $B_{i,j}$ and applying the divergence theorem gives

$$\int_{B_{i,j}} \frac{\partial n}{\partial t}\, dA = -\int_{B_{i,j}} \nabla \cdot \mathbf{f}\, dA = -\int_{\partial B_{i,j}} \mathbf{f} \cdot \mathbf{n}\, ds \tag{3.6}$$

where $\mathbf{n}$ is the outward normal vector of $B_{i,j}$. Since n is constant within the box and $\mathbf{f} \cdot \mathbf{n}$ is constant along box boundaries, this reduces to

$$\Delta x \Delta y \frac{\partial n_{i,j}}{\partial t} = -\Delta y \left(f^1_{i,j+\frac{1}{2}} - f^1_{i,j-\frac{1}{2}} \right) - \Delta x \left(f^2_{i+\frac{1}{2},j} - f^2_{i-\frac{1}{2},j} \right). \tag{3.7}$$

Dividing through by $\Delta x \Delta y$ gives the system of ordinary differential equations

$$\frac{d}{dt} n_{i,j} = -\frac{1}{\Delta x} \left(f^1_{i,j+\frac{1}{2}} - f^1_{i,j-\frac{1}{2}} \right) - \frac{1}{\Delta y} \left(f^2_{i+\frac{1}{2},j} - f^2_{i-\frac{1}{2},j} \right) \tag{3.8}$$

where the fluxes at the box boundary midpoints are

$$\begin{aligned} f^1_{i,j\pm\frac{1}{2}} &= \pm \frac{D}{\Delta x}(n_{i,j} - n_{i,j\pm1}) \pm \frac{z\mu}{2\Delta x}(n_{i,j} + n_{i,j\pm1})(\phi_{i,j} - \phi_{i,j\pm1}) \\ f^2_{i\pm\frac{1}{2},j} &= \pm \frac{D}{\Delta x}(n_{i,j} - n_{i\pm1,j}) \pm \frac{z\mu}{2\Delta x}(n_{i,j} + n_{i\pm1,j})(\phi_{i,j} - \phi_{i\pm1,j}). \end{aligned} \tag{3.9}$$

The same method can be applied to equation 2.2 to obtain the discretized system of linear equations for the potential,

$$\frac{1}{\Delta x^2}\left(\phi_{i,j-1} - 2\phi_{i,j} + \phi_{i,j+1}\right) + \frac{1}{\Delta y^2}\left(\phi_{i-1,j} - 2\phi_{i,j} + \phi_{i+1,j}\right) = -\rho_{i,j}/\varepsilon. \tag{3.10}$$

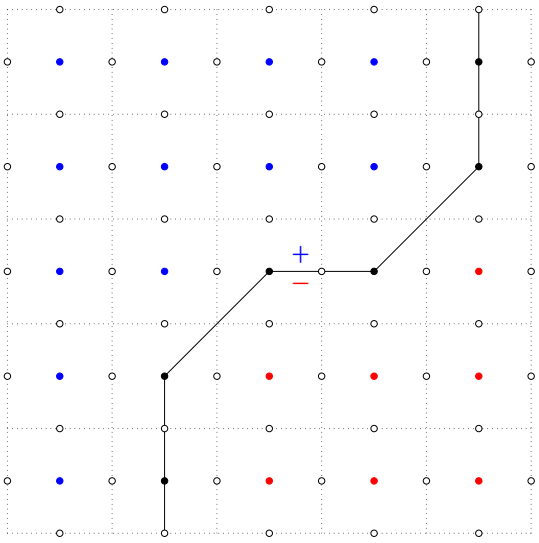

Figure 3.4: A diagram of the computational grid for demonstrating the box method. Extracellular points are colored red, intracellular points are colored blue and membrane boundary points are colored black. The solid line segments represent the membrane and the dashed lines represent the boxes. The open circles show the points where the flux is defined.

So far, the box appears to be equivalent to using a second-order finite difference method on a centered stencil. However, the box method offers an advantage over finite difference methods when deriving a conservative scheme for the membrane surface charge densities and for implementing the membrane boundary conditions of the potential.

Discretization of Surface Charge Density Equations

Recall the equation we use to model σ_i on the membrane

$$\frac{\partial \sigma_i^{\pm}}{\partial t} = -l_D^{\pm} \nabla \cdot \mathbf{j}_i^{\pm} \mp j_{m,i}. \tag{3.11}$$

Let B denote the box surrounding an arbitrary membrane point and $B^{\pm}$ denote the portion on the box on the $\pm$ side of the membrane. Integrating 3.11 over $B^{\pm}$ gives

$$\int_{B^{\pm}} \frac{\partial \sigma_i^{\pm}}{\partial t}\, dA = -l_D^{\pm} \int_{B^{\pm}} \nabla \cdot \mathbf{j}_i^{\pm}\, dA \mp \int_{B^{\pm}} j_{m,i}\, dA. \tag{3.12}$$

Applying the divergence theorem yields

$$\int_{B^\pm} \frac{\partial \sigma_i^\pm}{\partial t}\, dA = -l_D^\pm \int_{\partial B^\pm} \mathbf{j}_i^\pm \cdot \mathbf{n}\, ds \mp \int_{B^\pm} j_{m,i}\, dA. \tag{3.13}$$

Since $\sigma_i^\pm$ and $j_{m,i}$ are constant inside the box and $\mathbf{j}_i^\pm \cdot \mathbf{n}$ is constant along any segment of the box's boundary,

$$A^\pm \frac{\partial \sigma_i^\pm}{\partial t} = -l_D^\pm \sum_k \mathbf{j}_{i,k}^\pm \cdot \mathbf{n}_k s_k^\pm \mp A^\pm j_{m,i} \tag{3.14}$$

where k ranges over the four sides of B, $s_k^\pm$ is the length in which the kth side of B lies on the $\pm$ side of the membrane, $\mathbf{n}_k$ is the outward pointing unit normal vector on the kth side of B and $A^\pm$ is the area of $B^\pm$. We also introduce the notation $\mathbf{j}_{i,k}^\pm$ to represent the current flux of the ith ionic species on the $\pm$ side of the membrane, evaluated on the kth side of B. Dividing each side of equation 3.14 by $A^\pm$ gives the discretized ODE

$$\frac{d\sigma_i^\pm}{dt} = -\frac{l_D^\pm}{A^\pm} \sum_k \mathbf{j}_{i,k}^\pm \cdot \mathbf{n}_k s_k^\pm \mp j_{m,i}. \tag{3.15}$$

Note that when we evaluate the RHS of 3.15, we define $s_k^\pm = 0$ if side k is not on the $\pm$ side of the membrane.

Charge Neutrality Condition on Membranes

Lastly, we must use the box method to define the charge neutrality condition on the membranes to obtain an algebraic equation for ϕ^+ and ϕ^- that allows us to implement the membrane boundary conditions from equations 2.35 and 2.37. We begin by considering the condition from 2.37 on an arbitrary membrane boundary point:

$$[\mathbf{n}_m \cdot \nabla \phi] = 0. \tag{3.16}$$

In order to apply the box method, we can restate this as the equivalent charge neutrality condition

$$\nabla \cdot \nabla \phi = -\rho/\varepsilon = 0. \tag{3.17}$$

Integrating each side of this equation over the box B gives

$$\int_B \nabla \cdot \nabla \phi\, dA = \int_{B^+} \nabla \cdot \nabla \phi^+\, dA + \int_{B^-} \nabla \cdot \nabla \phi^-\, dA = 0 \tag{3.18}$$

Applying the divergence theorem, we have

$$\int_{\partial B^+} \nabla\phi^+ \cdot \mathbf{n}\, ds + \int_{\partial B^-} \nabla\phi^- \cdot \mathbf{n}\, ds = 0. \tag{3.19}$$

Since $\nabla\phi^+ \cdot \mathbf{n}$ and $\nabla\phi^- \cdot \mathbf{n}$ are constant along box boundaries, we have

$$\sum_k (\nabla\phi^+)_k \cdot \mathbf{n}_k s_k^+ + \sum_k (\nabla\phi^-)_k \cdot \mathbf{n}_k s_k^- = 0. \tag{3.20}$$

Now let us define a specific ordering for the index k such that

$$\mathbf{n}_1 = (1,0),\ \mathbf{n}_2 = (0,1),\ \mathbf{n}_3 = (-1,0),\ \mathbf{n}_4 = (0,-1). \tag{3.21}$$

Using this ordering and writing out the expression for $(\nabla\phi^\pm)_k \cdot \mathbf{n}_k$ for every k leads to an equation of the form

$$L^+\phi^+ + L^-\phi^- = P^+ + P^- \tag{3.22}$$

where

$$L^\pm = \frac{s_1^\pm + s_3^\pm}{\Delta x} + \frac{s_2^\pm + s_4^\pm}{\Delta y} \tag{3.23}$$

and

$$P^\pm = \frac{s_1^\pm \phi_{i,j+1} + s_3^\pm \phi_{i,j-1}}{\Delta x} + \frac{s_2^\pm \phi_{i+1,j} + s_4^\pm \phi_{i-1,j}}{\Delta y} \tag{3.24}$$

Combining this with the boundary condition from 2.35, we may solve for ϕ^+ and ϕ^- to get the numerical boundary conditions

$$\phi^- = \frac{P^+ + P^- - L^+\sigma/C_m}{L^+ + L^-} \tag{3.25}$$

$$\phi^+ = \phi^- + \frac{\sigma}{C_m}. \tag{3.26}$$

Computing Geometric Factors

To use this method, we must have a way of computing the geometric factors $A^\pm$ and $s_k^\pm$. For each point on the membrane, the factors are determined by the pair of adjacent membrane line segments. Given our algorithm to compute a meshed curve, there are 32 possible configurations for consecutive line segments, also taking orientation into account. However, there are only four

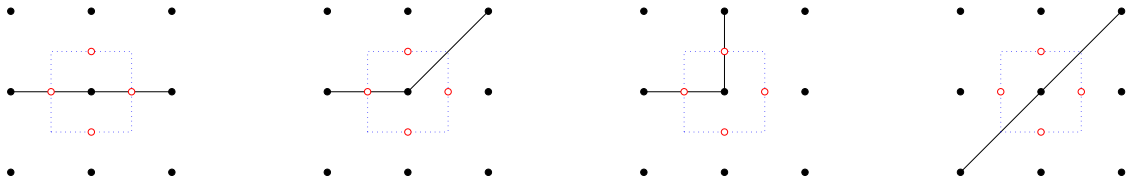

Figure 3.5: The four fundamental configurations of the meshed boundary curve.

fundamental configurations, shown in Figure 3.5, the rest being compositions of 90° rotations and vertical/horizontal flips of the these four configurations. From this figure, we see there are a limited number of values that $A^{\pm}$ and $s_k^{\pm}$ can have. In particular, $A^{\pm} = \alpha^{\pm}\Delta x\Delta y$ where $\alpha^{\pm} \in \{\frac{1}{4}, \frac{3}{8}, \frac{1}{2}, \frac{5}{8}, \frac{3}{4}\}$ is the fractional area of the box on the $\pm$ side and $s_k^{\pm} \in \{0, \frac{\Delta x}{2}, \frac{\Delta y}{2}, \Delta x, \Delta y\}$. For all boxes that do not intersect the outer boundary, $\alpha^+ + \alpha^- = 1$. For boxes that intersect the outer boundary, $\alpha^+ = \alpha^- = 1/4$. Since we use a static membrane that does not change in time, we only need to compute the geometric factors once during the initialization process and can use them throughout the rest of the simulation. To do this, we loop over the membrane points and determine which of the 32 cases each point belongs to and fill in the values of the geometric factors accordingly.

3.3 Temporal Discretization: TRBDF2

We now discuss the temporal discretization of the system of ordinary differential equations that arises from the spatial discretization discussed in the previous section. Suppose we include $N_{species}$ ionic species in the model and discretize the equations on a grid with N_{pts} points. Then equation the drift-diffusion transport equations from 2.9 become a system of $N_{species}N_{pts}$ nonlinear ordinary differential equations and the Poisson equation from 2.10 becomes a system of N_{pts} linear algebraic equations. The drift term causes the nonlinearity of 2.9 because it is coupled to equation 2.10 through the potential. Solving this coupled system would then require us to solve a system of $(N_{species}+1)N_{pts}$ nonlinear equations at every time level, which is an enormously expensive task when implementing an implicit method. However, if we assume that the potential is constant over any given time step, we can drastically reduce the computational cost

of the problem. By making this assumption, equations 2.9 and 2.10 decouple and can be solved independently. Further, 2.9 becomes linear since we use the potential at the previous time step. This results in a considerably cheaper overall scheme, but it is only semi-implicit so stability requirements limit the time step sizes we may use.

General Description

The method we use for the temporal discretization of 3.8 is known as the TRBDF2 method, developed by Bank et al. in [4]. The scheme is considered the state-of-the-art method for solving ODE systems arising from the spatial discretizations of parabolic PDEs. It is second order accurate, fully implicit and L-stable. For the sake of generality, we will demonstrate the method for an arbitrary function $u(t)$, without making any reference to the variables of our model.

Consider the system of N autonomous ordinary differential equations given by

$$\frac{du}{dt} = f(u), \;\; t > 0, \;\; u(t), f(u) \in \mathbb{R}^N$$

with an initial condition $u(0) = u_0$. We use the notation $u_k = u(t_k)$ where (t_k) is a finite sequence of t values where the solution is computed and $t_0 = 0$. Given u_k, we solve for u_{k+1}, the solution at the next time level, in two steps. We first compute an intermediary solution at time $t_k + \gamma \Delta t_k$ where $\gamma \in (0,1)$ using the trapezoid rule (TR):

$$u_{k+\gamma} = u_k + \frac{\gamma \Delta t_k}{2} \left[f(u_k) + f(u_{k+\gamma}) \right]. \tag{3.27}$$

Next we use the second-order backward difference formula (BDF2) to compute u_{k+1} in terms of u_k and $u_{k+\gamma}$:

$$u_{k+1} = \frac{1}{\gamma(2-\gamma)} u_{k+\gamma} - \frac{(1-\gamma)^2}{\gamma(2-\gamma)} u_k + \frac{1-\gamma}{2-\gamma} \Delta t_k \, f(u_{k+1}). \tag{3.28}$$

It can be shown via Taylor series expansions that the dominant term in the local truncation error (LTE) at time level k is

$$\text{LTE}_k = c(\gamma) \Delta t_k^3 u^{(3)}(t_k) \tag{3.29}$$

where

$$c(\gamma) = \frac{-3\gamma^2 + 4\gamma - 2}{12(2-\gamma)}. \tag{3.30}$$

We can now choose the optimal value of γ by finding the minimizer of $\|\text{LTE}_k\|$. This amounts to solving $c'(\gamma) = 0$ subject to the constraints $c''(\gamma) > 0$ and $\gamma \in (0,1)$. Such a solution exists and gives the optimal value $\gamma = 2 - \sqrt{2} \approx 0.5858$.

Dynamic Time Step Adjustment

When simulating large systems to steady state, it is necessary to implement a dynamically adjusted time step. To do this, we use a divided difference estimate to approximate the local truncation error of TRBDF2 as

$$\text{LTE}_{k+1} \approx 2c\Delta t_k \left(\frac{1}{\gamma} f(u_k) - \frac{1}{\gamma(1-\gamma)} f(u_{k+\gamma}) + \frac{1}{1-\gamma} f(u_{k+1}) \right) \tag{3.31}$$

which can then be used to adjust Δt_k accordingly. The typical algorithm for time step selection is to set

$$\Delta t_{k+1} = \Delta t_k r_{k+1}^{-1/(p+1)}, \quad r_{k+1} = \frac{\|\text{LTE}_{k+1}\|}{\varepsilon_R \|u_k\| + \varepsilon_A} \tag{3.32}$$

where $\|\cdot\|$ is the discrete L^1 norm, p is the order of the method ($p = 2$ for this case) and ε_R and ε_A are the relative and absolute error tolerances, respectively. If $r_{k+1} = O(1)$, then the norm of the LTE is on the same order as the most dominant term in the denominator, which means the time step is acceptable. The exact condition most commonly used in practice for an acceptable time step is to require $r_{k+1} \leq 2$. If this is the case, the solution is updated with that time step and a new (usually larger) time step is computed. Otherwise, the time step is adjusted (shrunk) and the solution is re-computed with the smaller time step. The major benefit to this method is when simulating to steady state, the time steps can become rather large, without loss in accuracy. In most of our simulations, we use $\varepsilon_R = 10^{-6}$ and $\varepsilon_A = 10^{-12}$, although they can be adjusted accordingly to yield higher accuracy (at the cost of smaller time steps).

3.4 Rectangular Poisson Solver

We now give a description of the numerical method used to solve the Possion equation from 2.10 in the rectangular domain. The method presented here is one of the fastest known methods to solve the Poisson equation and is particularly efficient in applications where the equation must be solved at every time step. Consider the Poisson equation $\nabla^2 u = f$ on an arbitrary rectangle in 2D with Dirichlet boundary conditions. Recall that our computational domain uses uniform grid spacing in each direction, but with possibly unequal Δx and Δy. Assume the domain is discretized into an $(M+1)\times(N+1)$ grid. The interior unknown solution can be treated as an $(M-1)\times(N-1)$ matrix (U_{ij}) where U_{ij} is the numerical approximation of $u(x_j, y_i)$. Using second order finite differences, we can state the discrete problem as the matrix equation

$$UA + BU = F \tag{3.33}$$

where A and B are square tridiagonal matrices, of sizes $N-1$ and $M-1$, respectively, given by

$$A = \frac{1}{\Delta x^2}\begin{bmatrix} -2 & 1 & & \\ 1 & -2 & \ddots & \\ & \ddots & \ddots & 1 \\ & & 1 & -2 \end{bmatrix}_{(N-1)\times(N-1)}, \; B = \frac{1}{\Delta y^2}\begin{bmatrix} -2 & 1 & & \\ 1 & -2 & \ddots & \\ & \ddots & \ddots & 1 \\ & & 1 & -2 \end{bmatrix}_{(M-1)\times(M-1)}.$$

The matrix F is the same size as U and contains the values of the function f along with boundary data. Both A and B have unique sets of eigenvalues and are therefore diagonalizable. Thus there exists a diagonal matrix D and an invertible matrix T such that $A = TDT^{-1}$. The entries of D and T are known analytically and can be shown to be

$$D_{kk} = \frac{1}{\Delta x^2}\left[2\cos(k\pi/N) - 2\right], \;\; k = 1, ..., N-1,$$

$$T_{jk} = \sin(jk\pi/N), \;\; j = 1, ..., M-1, \;\; k = 1, ..., N-1.$$

Similar formulas for B apply but we do not need them here. By diagonalizing A, equation 3.33 becomes

$$UTDT^{-1} + BU = F \Rightarrow UTD + BUT = FT \Rightarrow VD + BV = H$$

where $V = UT$ and $H = FT$. Since D is a diagonal matrix, this matrix equation decouples into $N-1$ independent linear systems, one for each column of V. Let V_k and H_k denote the kth columns of V and H, respectively. Then we get the set of tridiagonal linear systems

$$(D_{kk}I + B)V_k = H_k, \;\; k = 1, ..., N-1 \tag{3.34}$$

where I is an $M-1 \times M-1$ identity matrix. Using a specialized tridiagonal solver, each of these equations can quickly be solved to construct V column by column. The last step would be to set $U = VT^{-1}$. Note that this process could instead be applied by diagonalizing B and solving for each row of V. We also see from 3.34 that the condition for a unique solution to 3.33 is that $-D_{kk}$ can not be an eigenvalue of B for any $k = 1, ..., N-1$. However, for this particular problem, A and B are both negative definite, so the solution to 3.33 always exists.

This particular algorithm has many advantages over a direct linear solver, especially when f varies in time and we are required to solve Poisson's equation at every time level. Since T is only of size N, we may easily compute T^{-1} once before the time loop begins and then use it throughout the rest of the simulation. Assuming T and T^{-1} are available, the most expensive steps in this algorithm are computing $H = FT$ and $U = VT^{-1}$, which have $O(MN^2)$ run time. Solving the set of $N-1$ tridiagonal systems has a run time of only $O(MN)$. Moreover, the performance can be improved by considering the relative sizes of M and N. If we instead chose to diagonalize B, the algorithm run time would be $O(M^2N)$. Thus we can always get a run time of $O(\min\{M^2N, MN^2\})$ by choosing which matrix to diagonalize appropriately. Compared to a direct linear solver, which has a run time of $O(M^2N^2)$, this method is $\max\{M,N\}$ times faster.

3.5 Solving Equations: The SOR Method

With the spatial and temporal discretizations of the drift-diffusion equations 2.9 and 2.10 in hand, we now turn to the problem of solving the resulting system of linear algebraic equations. In the previous section, we demonstrated a very efficient method of solving Poisson's equation on a rectangular domain. However, when using a domain with complex geometry, such as the one shown in Figure 3.2, an iterative solver seems like the best choice, especially on a large grid.

The particular method we use is the SOR (successive over-relaxation) method with Chebyshev acceleration. We apply this method to solving the transport equation 2.9 in both the rectangular and complex domain and for solving the Poisson equation from 2.10 in the full synapse domain only.

General SOR Algorithm

To begin with, we give a general description of the SOR method with Chebyshev acceleration and then discuss its application to the specific equations from our model. The standard treatment of the SOR method is to consider a linear system and perform a certain splitting of the coefficient matrix. However, we will take a different approach by considering the method in "component" form, without reference to a coefficient matrix.

Let u be any function defined on the grid and suppose we want to solve the system of linear equations $F_{i,j}(u) = 0$ for every non-boundary grid point (x_j, y_i). Each of these equations will contain at most five terms since we are using a five point stencil. We can then write

$$F_{i,j}(u) = a_{i,j}u_{i,j} + b_{i,j}(u) \tag{3.35}$$

where $b_{i,j}(u)$ contains the four terms corresponding to the nearest neighbors of grid point (x_j, y_i). Starting with an initial guess for the solution, $u_{i,j}^{(0)}$, the iterates of the SOR method are defined as

$$u_{i,j}^{(p+1)} = u_{i,j}^{(p)} - \omega F_{i,j}(u^{(p)})/a_{i,j}, \quad p = 0, 1, 2, ... \tag{3.36}$$

where $\omega \in [1, 2)$ is an acceleration parameter used to speed up convergence, which is discussed further in the next subsection. Note that if $\omega = 1$, then equation 3.36 defines the Gauss-Seidel iteration. The residual of each iteration is defined as

$$r^{(p)} = \frac{1}{N_{pts}} \sum_{i,j} |F_{i,j}(u^{(p)})|. \tag{3.37}$$

The iterations are repeated until $r^{(p)} < \delta$ for some tolerance parameter δ. Clearly, we see from equation 3.36 that this method is only valid when $a_{i,j} \neq 0$ for all grid points. Although this

method is not always the fastest way to solve a linear system, it is particularly convenient for performing simulations on complicated grids. Applying the SOR method to a general system of linear equations, $F_{i,j}(u) = 0$, only requires us to compute the corresponding $a_{i,j}$ and $b_{i,j}(u)$ from the form defined in equation 3.35. We will later derive these expressions for all of the equations that we apply the method to.

Chebyshev Acceleration

The idea of Chebyshev acceleration is to adjust ω within each iteration of the SOR method in such a way that consistently decreases the residual. One possible implementation is to perform a red/black ordering of the grid points analogous to that of a checkerboard. In this arrangement, red points only couple to black points and vice verse. Each color has its own version of ω, which is adjusted within each iteration. The algorithm is to set

$$\begin{aligned} \omega_{red}^{(0)} &= 1 \\ \omega_{black}^{(0)} &= 1/(1-\rho_J^2/2) \\ \omega_{red}^{(p+1)} &= 1/(1-\rho_J^2\omega_{black}^{(p)}/4) \\ \omega_{black}^{(p+1)} &= 1/(1-\rho_J^2\omega_{red}^{(p+1)}/4) \end{aligned} \tag{3.38}$$

where ρ_J is the spectral radius of the Jacobian iteration matrix J. Empirical simulation data suggests that, for our problem, Chebyshev acceleration reduces the number of required iterations by about 15% on average, resulting in a non-trivial savings in overall computational cost.

Application to Conservation Equations

We now derive the expressions for $F_{i,j}$, $a_{i,j}$ and $b_{i,j}$ needed to apply the SOR method when solving the TRBDF2 equations for the particle densities. Recall the spatially discretized version

of equation 2.9 for an arbitrary ionic species n at the grid point (x_j, y_i):

$$\frac{d}{dt}n_{i,j} = -\frac{1}{\Delta x}\left(f^1_{i,j+1/2} - f^1_{i,j-1/2}\right) - \frac{1}{\Delta y}\left(f^2_{i+1/2,j} - f^2_{i-1/2,j}\right) \equiv G_{i,j}(n). \tag{3.39}$$

Since we treat the potential as remaining constant over any time step, we know that $G_{i,j}(n)$ is a linear function and that it is stated in terms of variables defined at (x_j, y_i) and the nearest neighbors of this point. We can thus write the functions $G_{i,j}(n)$ in the form

$$G_{i,j}(n) = A_{i,j}n_{i,j} + B_{i,j}(n). \tag{3.40}$$

By plugging in the expressions for the fluxes into the discretized equations, we see that

$$A_{i,j} = -2D\left(\frac{1}{\Delta x^2} + \frac{1}{\Delta y^2}\right) + \frac{z\mu}{2}\left[\frac{1}{\Delta x^2}(\phi_{i,j-1} - 2\phi_{i,j} + \phi_{i,j+1}) + \frac{1}{\Delta y^2}(\phi_{i-1,j} - 2\phi_{i,j} + \phi_{i+1,j})\right] \tag{3.41}$$

and

$$\begin{aligned} B_{i,j}(n) = &\frac{1}{\Delta x^2}\left[\left(D + \frac{z\mu}{2}(\phi_{i,j-1} - \phi_{i,j})\right)n_{i,j-1} + \left(D + \frac{z\mu}{2}(\phi_{i,j+1} - \phi_{i,j})\right)n_{i,j+1}\right] \\ &+ \frac{1}{\Delta y^2}\left[\left(D + \frac{z\mu}{2}(\phi_{i-1,j} - \phi_{i,j})\right)n_{i-1,j} + \left(D + \frac{z\mu}{2}(\phi_{i+1,j} - \phi_{i,j})\right)n_{i+1,j}\right]. \end{aligned} \tag{3.42}$$

We now want to combine the above formulas with the TRBDF2 update equations at time level k. Let us denote $n^k_{i,j}$ to be the solution at grid point (x_j, y_i) at time t_k. For the TR step, we wish to find the roots of the functions $F_{i,j}(n^{k+\gamma})$ defined by

$$F_{i,j}(n^{k+\gamma}) = n^{k+\gamma}_{i,j} - n^k_{i,j} - \gamma\frac{\Delta t_k}{2}\left(G^k_{i,j} + A_{i,j}n^{k+\gamma}_{i,j} + B_{i,j}(n^{k+\gamma})\right) = a_{i,j}n^{k+\gamma}_{i.j} + b_{i,j}(n^{k+\gamma}) \tag{3.43}$$

where

$$a_{i,j} = 1 - \gamma\frac{\Delta t_k}{2}A_{i,j} \tag{3.44}$$

and

$$b_{i,j}(n^{k+\gamma}) = -n^k_{i,j} - \gamma\frac{\Delta t_k}{2}\left(G^k_{i,j} + B_{i,j}(n^{k+\gamma})\right). \tag{3.45}$$

The initial guess for the TR step is taken to be n^k. Similarly, for the BDF2 step, we have

$$F_{i,j}(n^{k+1}) = n^{k+1}_{i,j} - \frac{1}{\gamma(2-\gamma)}n^{k+\gamma}_{i,j} + \frac{(1-\gamma)^2}{\gamma(2-\gamma)}n^k_{i,j} - \frac{1-\gamma}{2-\gamma}\Delta t_k(A_{i,j}n^{k+1}_{i,j} + B_{i,j}(n^{k+1})) \tag{3.46}$$

and can define

$$a_{i,j} = 1 - \frac{1-\gamma}{2-\gamma}\Delta t_k A_{i,j} \tag{3.47}$$

and

$$b_{i,j}(n^{k+1}) = -\frac{1}{\gamma(2-\gamma)}n_{i,j}^{k+\gamma} + \frac{(1-\gamma)^2}{\gamma(2-\gamma)}n_{i,j}^{k} - \frac{1-\gamma}{2-\gamma}\Delta t_k B_{i,j}(n^{k+1}). \tag{3.48}$$

The initial guess for the BDF2 step is $n^{k+\gamma}$.

Application to the Poisson Equation

To solve the discretized Poisson equation at time level k using SOR, we define

$$F_{i,j}(\phi^k) = \frac{1}{\Delta x^2}\left(\phi_{i,j-1}^k - 2\phi_{i,j}^k + \phi_{i,j+1}^k\right) + \frac{1}{\Delta y^2}\left(\phi_{i-1,j}^k - 2\phi_{i,j}^k + \phi_{i+1,j}^k\right) + \rho_{i,j}^k/\varepsilon \tag{3.49}$$

which immediately gives us

$$a_{i,j} = -2\left(\frac{1}{\Delta x^2} + \frac{1}{\Delta y^2}\right) \tag{3.50}$$

and

$$b_{i,j}(\phi^k) = \frac{1}{\Delta x^2}\left(\phi_{i,j-1}^k + \phi_{i,j+1}^k\right) + \frac{1}{\Delta y^2}\left(\phi_{i-1,j}^k + \phi_{i+1,j}^k\right) + \rho_{i,j}^k/\varepsilon. \tag{3.51}$$

3.6 Implementation

The program to simulate our model was written in the C language. There are five main structures that contain all the relevant data: ION, STATE, MEMSTATE, GRID and TIMESTEP. The ION structure contains all information relevant to a single ion species, such as its density, ionic charge, bath values, diffusion coefficient, etc. The STATE structure stores the potential and an array of IONS. The MEMSTATE structure stores all quantities defined only on membranes such as $\sigma_i^{\pm}$, $\phi^{\pm}, n_i^{\pm}$, etc. The GRID structure stores all information relevant to the geometry of the computational region such as the labeling matrix, mesh spacing, outer bounds for the region, etc. The TIMESTEP structure stores all information relevant to time step selection such ε_R, ε_A, etc.

To summarize the steps in implementing the solution, pseudocode for the main structure of the program is shown below.

- `initialize all variables`
- `while(not in steady state)`
    - `solve for the potential using SOR`
    - `solve for the updated particle densities using TRBDF2/SOR`
    - `compute all transmembrane current densities`
    - `compute surface charge densities on membranes with the box method`
    - `update the potential and particle densities on the membranes`
    - `implement the outer boundary conditions`
    - $\mathtt{t} \rightarrow \mathtt{t} + \Delta\mathtt{t}$

Note that the termination criteria of the while loop depends on whether the system has reached steady state or not. The system is deemed to be in steady state when the discrete L^1 norm of the time derivatives for all state variables falls under a certain threshold value, denoted as STOP. In our simulations, we used STOP $= 10^{-4}$.

The double-valued nature of the state variables on the membranes must be implemented with care since the solution matrix for any variable can only have one value at a time and the iterative solvers must couple to these values correctly. This is done by storing the $\pm$ values of the variables in separate arrays and then filling in the values of the solution matrix appropriately. For instance, when solving for the potential, we first fill in the ϕ^- values along the membranes and then iterate the extracellular points to convergence. Once this is done, we fill in the ϕ^+ values along the membranes and then iterate the intracellular points to convergence. The same process is applied to the ion densities as well.

To analyze the program's performance, we computed the fraction of the total CPU time used on a 600×900 grid for each of the functions listed above. The result was: 70% solving for ϕ, 29% solving for the ions and the remaining 1% to compute σ_i and update the boundaries. Therefore the main computational bottleneck is solving for ϕ. Since ion densities remain nearly constant away from the membranes, they only require a few iterations to converge. However, the potential varies much more and therefore can require 100-200 iterations to converge, making it the most expensive quantity to compute.

To increase performance, we used the OpenMP software for parallelizing some of the loops that occur within the computational bottlenecks. If the computations performed within a `for` loop are independent of one another with respect to the loop variable, OpenMP can split the iteration space into multiple threads and run them on different processors simultaneously. An interesting trick when implementing the SOR method is to split the `for` loop that iterates over grid points into multiple threads, each with their own memory space, but keep the grid variable in the shared memory spaced so it can be accessed by all threads. If all points were updated simultaneously, this method would reduce to an accelerated Jacobi method. However, since the workload among the processors is slightly unbalanced, points get updated in a random order, resulting in a form of chaotic relaxation. When using these methods on N processors, we observe a sub-linear relationship between the speed-up factor and N. For small N, the speed-up factor is about $N/2$ but this saturates as N is increased due to the poor scaling properties of shared address space parallel implementation. For example, when $N = 8$, we observe a speed-up factor of about 4 but when $N = 24$, we get a speed-up factor of about 8.

Note that this C program is independent of the geometry of the region we wish to use. All of the information pertaining to the grid is stored in text files that are read in by the program. This allows us to use the convenient MATLAB libraries to pre-process all of the grid data beforehand. We can also run simulations on different geometries without ever altering the C code.

Chapter 4

SIMULATION RESULTS

4.1 Rectangular Geometry

During the first phase of this research, we simulated our model on the rectangular region shown in Figure 3.1. Figures 4.1, 4.2, and 4.3 show the steady state surface plots of the various state variables using a 50×500 grid ($\Delta x = \Delta y = 0.8 \approx l_D^-$). The unknown biological parameters used for the rectangular problem are shown in Table 4.1. Note that these parameters were tuned within a physiologically relevant range to get the best fit with experimental data.

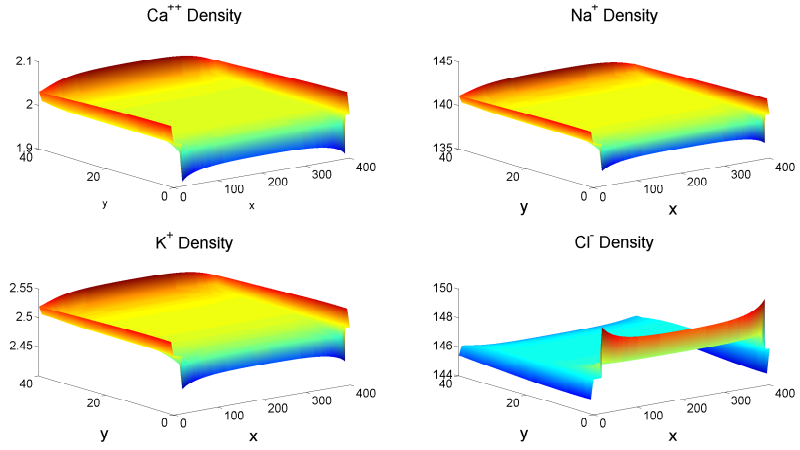

Figure 4.1: Steady state ion particle densities on the rectangular domain. Length units are shown in nanometers and the particle densities are shown in units of mM (10^{-3} moles/liter).

For these particular simulations, we used $\phi_{CP}^{+} = -80$ mV and $\phi_{HC}^{+} = -40$ mV. Figure 4.1 shows the particle densities for each ion. Boundary layers on the order of a Debye length appear near the membranes for each ion, which are consistent with the electric potential, shown in Figure 4.2. Away from the membranes, the particle densities are nearly constant at their bath values. Figure 4.3 shows the total charge density $\rho = \sum_i q_i n_i$, which is zero away from the membranes, as expected, but with charge layers near membranes.

Although the quantities shown in Figures 4.1, 4.2, and 4.3 help to validate certain physical properties we expect from the model, they are not quantities which are experimentally mea-

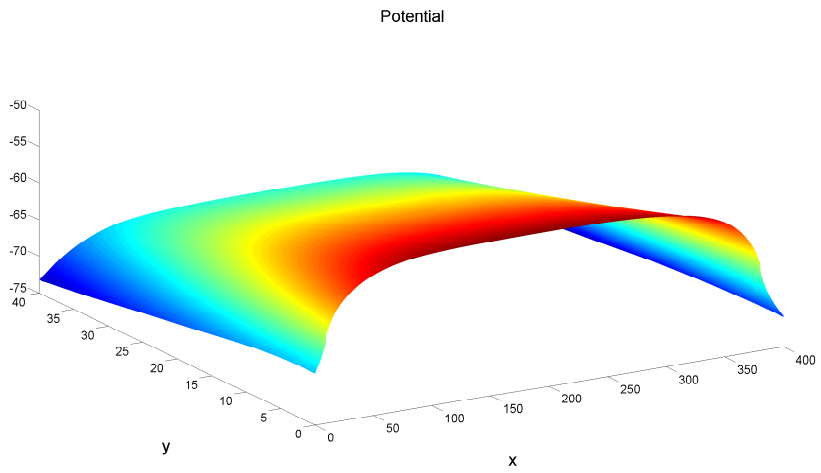

Figure 4.2: Steady state potential on the rectangular domain. Length units are shown in nanometers and the potential is shown in units of mV.

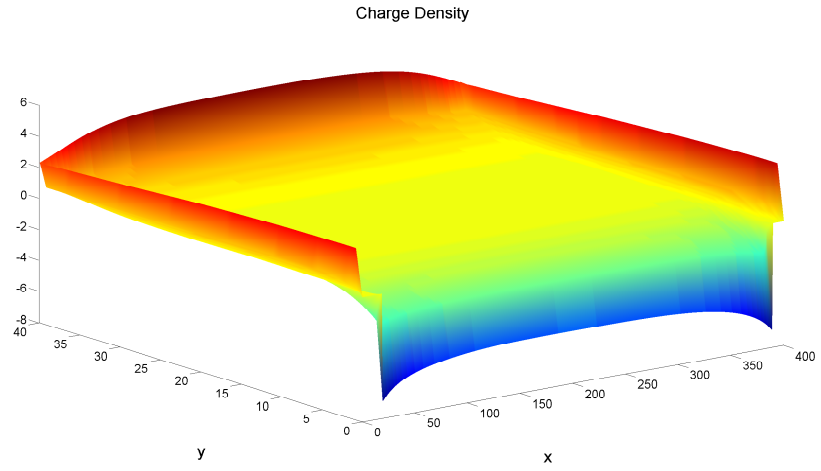

Figure 4.3: Steady state charge density on the rectangular domain. Length units are shown in nanometers and the charge density is shown in units of e·mM.

surable. In order to compare our simulations with experimental data, we computed the steady state current-voltage (IV) curves, which *are* measurable using voltage clamp techniques. In particular, we are interested in the relative shifts of the IV curves with and without background illumination as this demonstrates the feedback from horizontal cells to cones. The experimental data we use to compare our simulations with is from the goldfish experiments by Kamermans et al. in [45]. To produce the IV curves, we vary ϕ_{CP}^{+} over a range large enough such that $V_{CP} = \phi_{CP}^{+} - \phi^{-} \in [-70, 10]$ mV, since this is the range of the membrane potential seen in the

goldfish experiments. For a given value of ϕ_{CP}^{+}, we simulate to steady state and then use equation 2.33 to integrate $j_{m,Ca}$ over the membrane to obtain the total current I_{Ca} which provides a data point (V_{CP}, I_{Ca}) for the IV curve. The fitted parameters from Table 4.1 can affect the shape of the IV curve but all changes occur continuously as a function of the parameters, as can be inferred from the form of equation for I_{Ca}.

The computational domain used for this problem does not provide any natural region to treat as the potential ground. For this reason, simulating the background illumination through first principles, i.e., hyperpolarizing the horizontal cell membrane, is not particularly useful since it simply shifts the entire solution as if we just re-defined ground. Therefore, to simulate the background illumination, we adjust the kinetic parameter θ, resulting in two possible values, denoted as $\theta_{\pm}$, as shown in Table 4.1. As discussed earlier, we can view the formula for the transmembrane calcium current as a nonlinear form of Ohm's law that includes a sigmoidal shaped probability factor, otherwise known as an activation curve. The experimental data suggest that this activation curve gets shifted to more negative potentials when background illumination is present, which served as our inspiration to use this approach.

Parameter	Value	Units	Description
$g_{Ca,CP}$	1.5	nS	maximum conductance of calcium channels
$E_{Ca,CP}$	37	mV	reversal potential of calcium
λ	5	mV	kinetic parameter
θ_{+}	-33	mV	kinetic parameter, background off
θ_{-}	-40	mV	kinetic parameter, background on

Table 4.1: Calcium channel parameters used in simulations on the rectangular region.

As shown in Figure 4.4, the background illumination causes a shift in the IV curve and the magnitude of this shift indicates the strength of the feedback. An important feature of the ephaptic hypothesis is the idea that the feedback strength depends on how narrow the space between membranes is. To put this idea to the test, we performed a numerical experiment consisting of measuring the vertical shift in the IV curves with and without background illumination for three different sizes of the side openings. Figure 4.5 shows the results using the opening

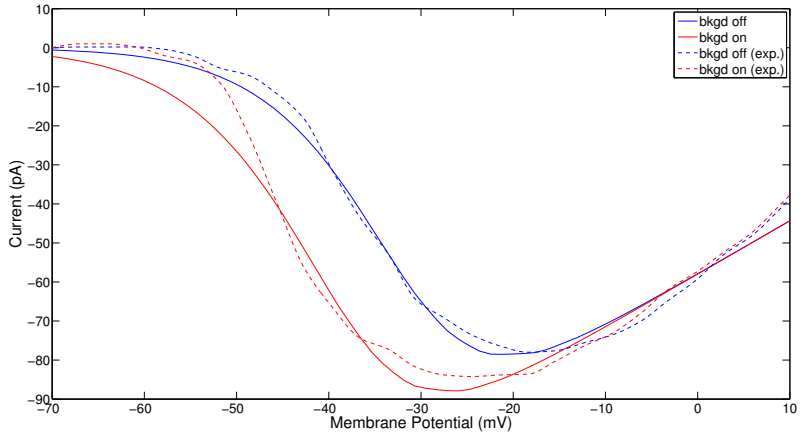

Figure 4.4: Steady state current-voltage curves with and without background illumination. The experimental curves are shown in dotted lines for reference.

widths 10/20 nm, 20/40 nm and 40/80 nm. This result shows that the maximum shift in the IV curves decrease as the widths of the openings increase.

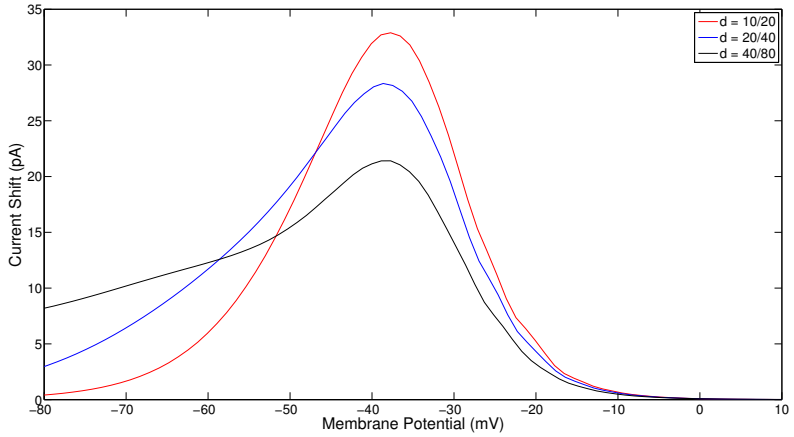

Figure 4.5: The vertical shift in the IV curves for different widths of the side openings demonstrates a critical aspect of the ephaptic hypothesis.

The model for the cone calcium transmembrane current density $j_{m,Ca}$ is a phenomenological fitting curve, with $\theta_+ - \theta_-$ representing the nonlocal effect of hyperpolarization of the horizontal cell when the background illumination is turned on. The calcium current ought to couple locally to only the electric potential, which is modified globally by the horizontal cell's hyperpolarization. Inserting the reference voltage in the complex 2D geometry of the synapse

allows us to model the effects of the hyperpolarization of the horizontal cell on the cone calcium transmembrane current at a microscopic level through the drift-diffusion model.

4.2 Full Synapse Geometry

We now present the results from simulations on the grid with the full synapse geometry. One crucial difference in our methodology for this problem, as opposed to the rectangular problem, is that the background illumination is simulated by adjusting the holding potential inside the horizontal cell, not by changing the value of the kinetic parameter θ. With this grid, we have a well-defined reference point for the potential, which now gives meaning to shifting the horizontal cell holding potential. As mentioned in the introduction, background illumination hyperpolarized the horizontal cell. Thus, in all simulations, we use $U_{HC} = -40$ mV to simulate without background illumination and $U_{HC} = -60$ mV to simulate with background illumination. The reference potential is held at $U_{ref} = -40$ mV for all simulations. The unknown biological parameters used for the full synapse geometry are shown in Table 4.2. Again, these parameters were tuned within a physiologically relevant range to get the best fit with experimental data.

Parameter	Value	Units	Description
$g_{Ca,CP}$	2.2	nS	maximum conductance of calcium channels
$E_{Ca,CP}$	50	mV	reversal potential of calcium
λ	3	mV	kinetic parameter
θ	5	mV	kinetic parameter

Table 4.2: Calcium channel parameters used in simulations for the full synapse geometry.

In Figures 4.6, 4.7, 4.8 and 4.9, we show color plots of the steady state potential on a 600×900 grid, with and without background illumination, using several different values for U_{CP}. To get a good view of the charge layers, we zoom in on the region containing the channels and plot the steady state charge density as shown in Figure 4.10. This figure verifies that the baths remain charge neutral away from the membranes and the charge layers that accumulate on each side are equal in magnitude but opposite in sign, i.e., the membrane also maintains overall neutrality.

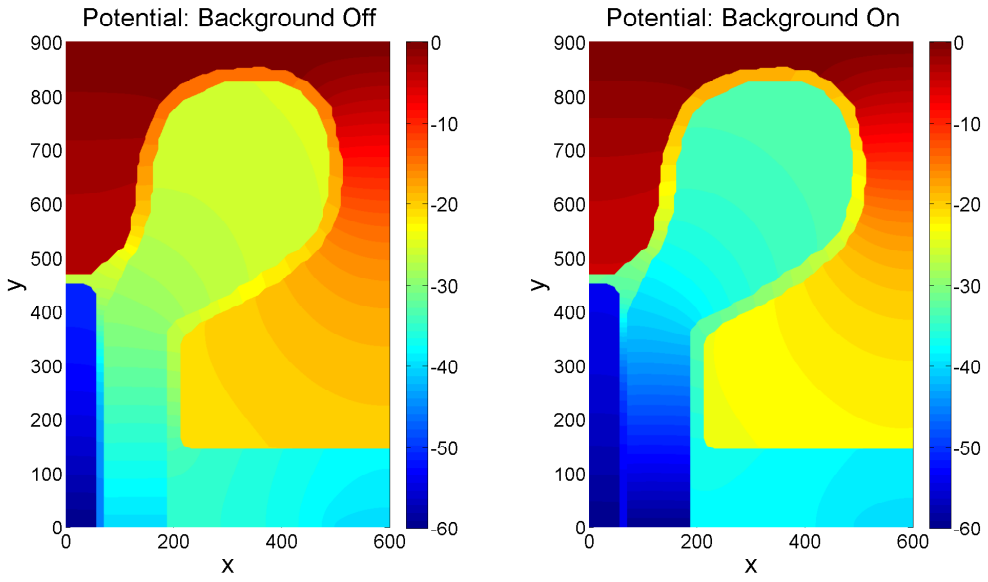

Figure 4.6: Steady state potential in the full synapse geometry with $U_{CP} = 0$ mV and $U_{BC} = -60$ mV. Lengths are in units of nanometers and the potential is shown in units of mV.

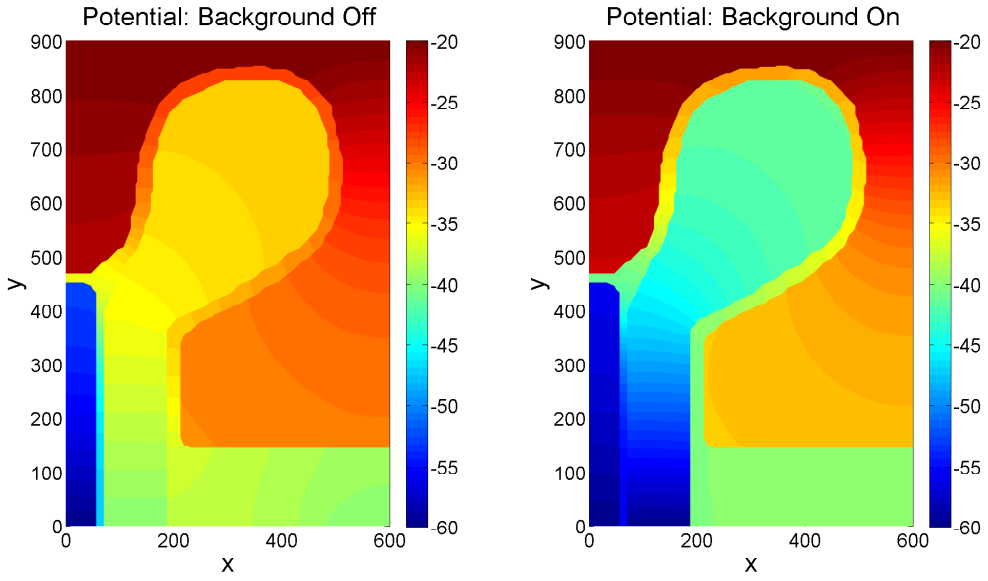

Figure 4.7: Steady state potential in the full synapse geometry with $U_{CP} = -20$ mV and $U_{BC} = -60$ mV. Lengths are in units of nanometers and the potential is shown in units of mV.

To verify that our numerical method for implementing the jump conditions on the potential enforces charge neutrality on the membranes, we plot $\sigma^+ = \sum_i \sigma_i^+$ and $\sigma^- = \sum_i \sigma_i^-$ in Figure 4.11. The horizontal axes in these plots represent the interior boundary curves with a clockwise orientation with respect to the normal vector pointing from the $+$ side to the $-$ side

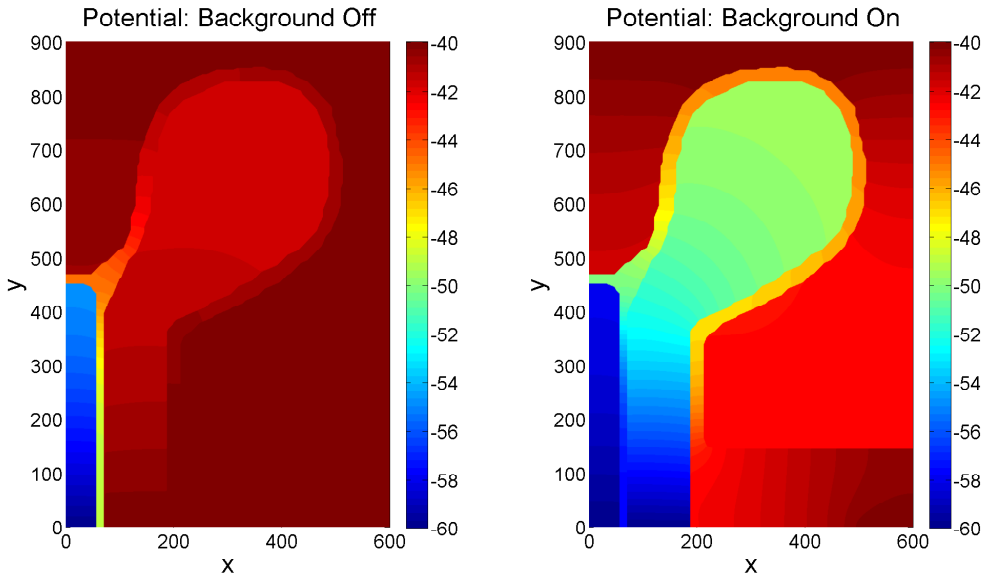

Figure 4.8: Steady state potential in the full synapse geometry with $U_{CP} = -40$ mV and $U_{BC} = -60$ mV. Lengths are in units of nanometers and the potential is shown in units of mV.

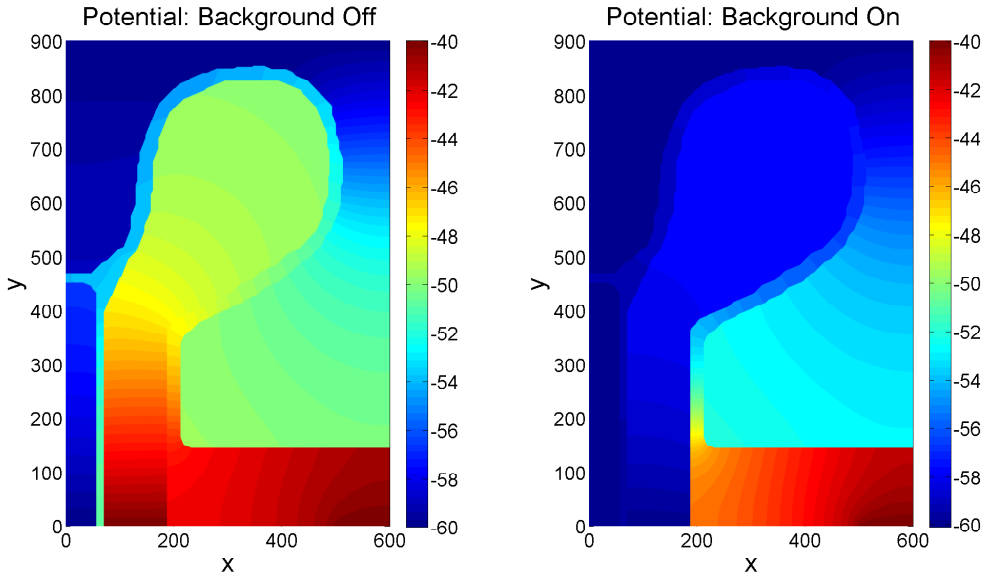

Figure 4.9: Steady state potential in the full synapse geometry with $U_{CP} = -60$ mV and $U_{BC} = -60$ mV. Lengths are in units of nanometers and the potential is shown in units of mV.

of the membranes. Indeed, we see that $\sigma^+ = -\sigma^-$ everywhere, with an error on the order of the double precision machine epsilon.

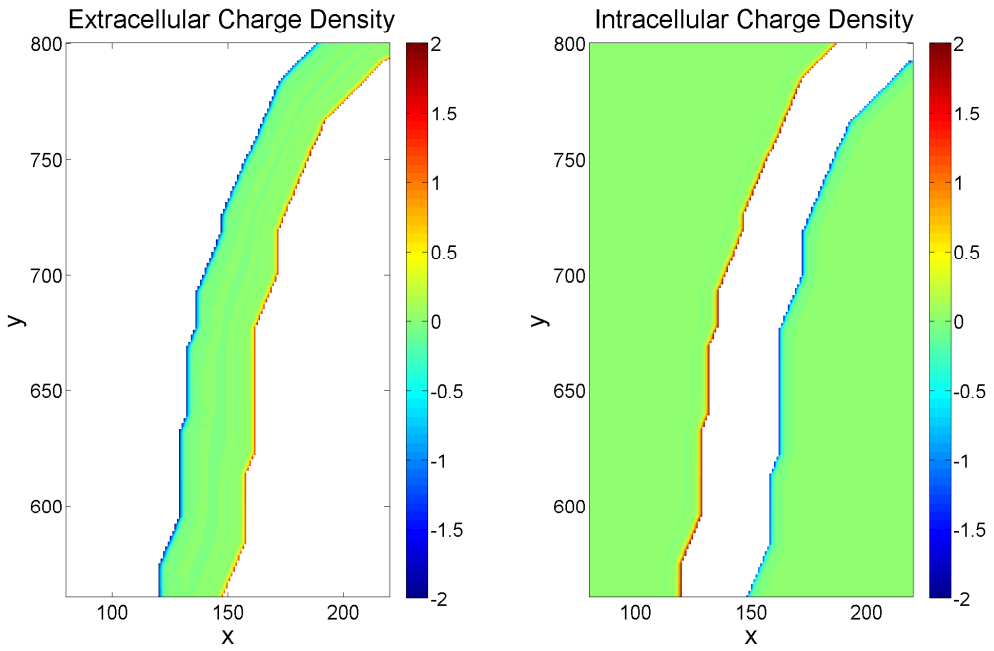

Figure 4.10: A zoomed-in view of the steady state charge density along the portion of the membranes containing ion channels with $U_{CP} = -20$ mV, $U_{HC} = -40$ mV and $U_{BC} = -60$ mV. Lengths are in units of nanometers and the charge density is shown in units of e·mM.

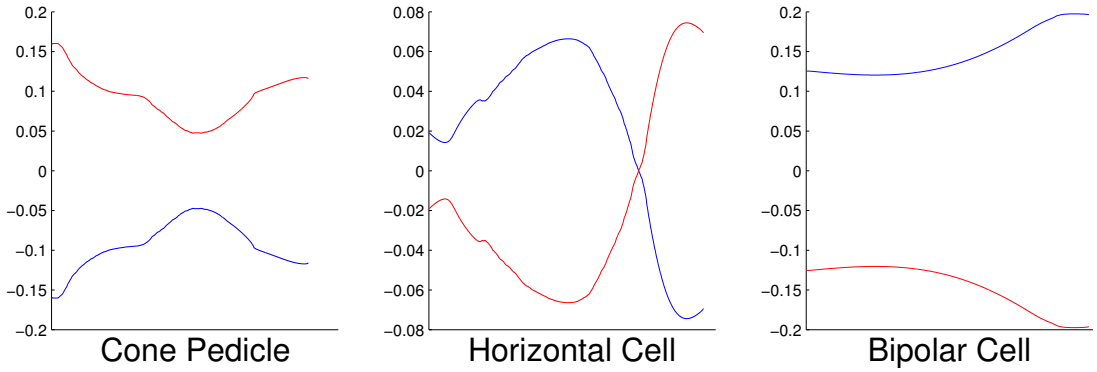

Figure 4.11: Steady state surface charge density along the membranes, shown in units of e/nm^2. The blue curves show σ^- and the red curves show σ^+. The holding potentials used for this simulation are $U_{CP} = -20$ mV, $U_{HC} = -40$ mV and $U_{BC} = -60$ mV.

As with the rectangular geometry, we produced IV curves with and without background illumination to observe how the model predicts the feedback response. The IV curves are generated by varying U_{CP} over the range $[-80, 10]$ mV and then computing the current I_{Ca} in steady state to get a data point (U_{CP}, I_{Ca}). Since this requires us to run about 30 simulations for various values of U_{CP}, we use a coarse 150×225 grid.

The addition of the bipolar cell slightly complicates things. Some bipolar cells are known to depolarize under background illumination (OFF bipolar cells) and others are known to hyperpolarize under background illumination (ON bipolar cells). To understand how the holding potential of the bipolar cell affects the IV curves, we tried three different cases, which we label neutral, depolarized and hyperpolarized. For all three cases, we use $U_{BC} = -60$ mV with no background illumination. When the background illumination is present, we use $U_{BC} = -60$ mV, $U_{BC} = -40$ mV and $U_{BC} = -80$ mV for the neutral, depolarized and hyperpolarized cases, respectively. Figure 4.12 shows the results for all three cases along with the vertical shift in the IV curves. This figure indicates that the shift in the IV curves is enhanced when the bipolar cell is hyperpolarized and reduced when the bipolar cell is depolarized.

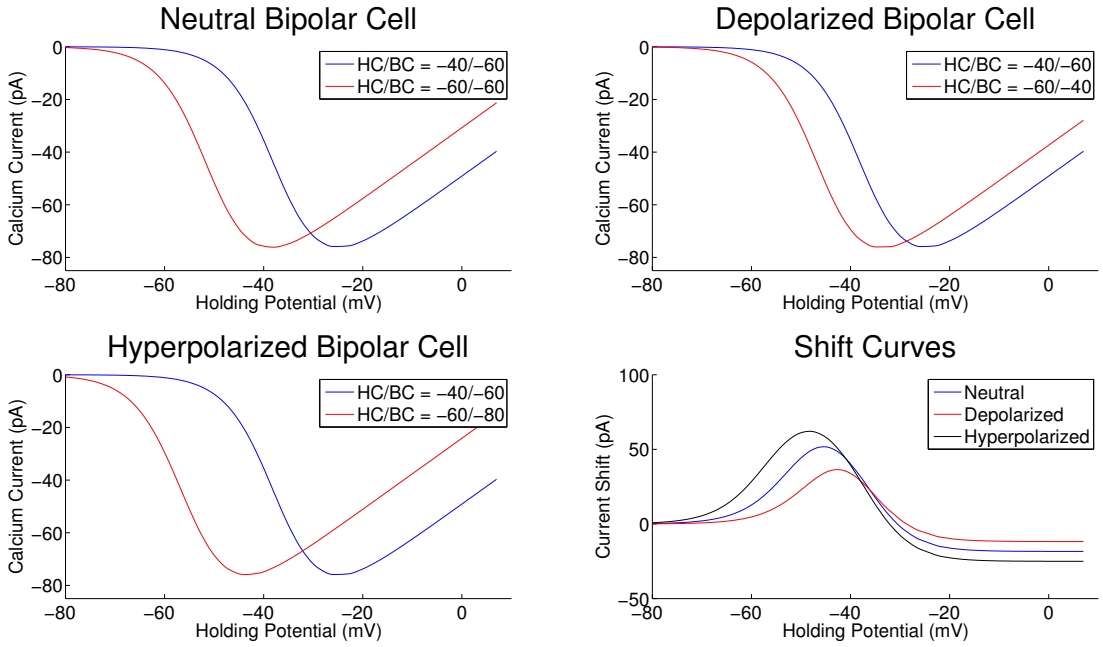

Figure 4.12: Steady state current-voltage curves for different bipolar cell holding potentials. *Top-left*: Neutral bipolar cell. *Top-right*: Depolarized bipolar cell. *Bottom-left*: Hyperpolarized bipolar cell. *Bottom-right*: Vertical difference of IV curves for all three cases.

Chapter 5

CONCLUSION & FUTURE WORK

5.1 Conclusion

The results of our simulations provide convincing evidence for the ephaptic hypothesis. The simulations performed on the rectangular region for variable inlet/outlet opening widths demonstrate the importance of the geometry of the triad synapse. The magnitude of feedback from horizontal cells to cone is quantified by the maximum shift in the IV curves with and without background illumination. As shown in Figure 4.5, this shift is increased as the width of the openings are decreased. When ionic currents travel through these narrow regions of high resistance, they create a large potential drop which can ultimately cause global changes in the potential and in the distribution of charge which in turn affects the flow of calcium into the cone pedicle.

The most convincing evidence for the ephaptic hypothesis provided by our simulations is the shifting of the IV curves in the full synapse geometry with and without background illumination. This shift characterizes the feedback from horizontal cells to cones and it was produced simply by hyperpolarizing the horizontal cell holding potential, without using any chemical transmitters or pH mechanisms. This is a strong indication that the feedback mechanism is dominated by electrical effects and other mechanisms are of secondary importance.

The simulations in the full synapse geometry also demonstrate the dependence of the feedback on the behavior of the bipolar cell under background illumination. The neutral case, shown in the upper left subfigure of Figure 4.12 appears to be the closest match with the experimental data from [45]. Since experiments measure currents for an entire cone pedicle with multiple triad synapses, our results suggest that there is approximately an equal number of ON and OFF bipolar cells in a given pedicle, which serve to balance out the shift effects. This result could be experimentally verified by blocking the ON bipolar cells with a chemical inhibitor, which would recover the contribution of the OFF biploar cells only.

Previous models to study the feedback phenomena in the triad synapse have been mostly compartment models in which each cell and the extracellular space are treated as isopotential regions. Given the amount of variation in the potential within the different compartments, shown in Figures 4.6, 4.7, 4.8 and 4.9, it is clear that compartment models are often insufficient in providing detailed and accurate physical insights. Although there are applications in neuroscience where compartment models have enjoyed much success in making accurate predictions, problems involving highly complex geometries require a more detailed spatial model, such as the one provided here. Such detailed models are often considered impractical because of their computational cost but as computing science continues to move forward, these models become more practical. Ultimately, to gain a complete understanding of electrical mechanisms in neuroscience, detailed models such as the one presented here will become necessities in the future.

5.2 Future Work

There are many directions for possible future work in this area. The general model we developed here for ionic flow and membrane dynamics could be applied to a large number of existing and future problems in computational neuroscience. From a numerical methods perspective, it would be interesting to see the box method we developed here for handling double-valued interior boundaries generalized to 3D. There are also several additions and improvements that can be made to our model for the triad synapse.

Although we were able to demonstrate the existence of electrical feedback in the triad synapse, we were not able to demonstrate the crucial role of the hemichannels in controlling this feedback. We believe this is due to our over-simplification of the transmembrane current models. A more comprehensive model should seek to improve upon this by modeling the channel dynamics from first principles, such as a Hodgkin-Huxley like model.

In addition, it may be possible to include the other proposed feedback mechanisms such as GABA transport and pH effects into the model to see how much they affect feedback. Testing

the effects of GABA could be done by including GABA as an extra "ion" species in the drift-diffusion equations but with a separate model for membrane dynamics. Testing pH effects would consist of adding in H^+ ions to the drift-diffusion equations, again with a separate model for membrane dynamics. The difficulty in adding these other mechanisms is the disparate time scales in which the dynamics occur. Electrical effects occur on time scales of microseconds whereas pH and GABA effects occur on much larger time scales such as milliseconds or even seconds. Thus a multiple time scale model would be necessary to correctly simulate all of these effects.

The work done in [3] derives a mathematical model for the electrical and chemical dynamics in the outer plexiform layer on large spatial and temporal scales which allows for simulation of time-dependent light flickering. Another possible future direction for this research is to combine features of this large scale model with our small scale model into one multi-scale model using homogenization techniques.

REFERENCES

[1] G. S. Ayoub, D. M. K. Lam. The content and release of endogenous GABA in isolated horizontal cells of the goldfish retina. *Vision Research*, 25(9): 11871193, 1985.

[2] N. Babai, W. B. Thoreson. Horizontal cell feedback regulates calcium currents and intracellular calcium levels in rod photoreceptors of salamander and mouse retina. *J. Physiol.*, 587(10): 23532364, 2009.

[3] S. M. Baer, S. Chang, S. M. Crook, C. L. Gardner, J. R. Jones, C. Ringhofer. Computational study of the cone-horizontal cell feedback mechanism in the outer-plexiform layer of cat retina. In progress.

[4] R. E. Bank, W. M. Coughran, W. Fichtner, E. H. Grosse, D. J. Rose, and R. K. Smith. Transient Simulation of Silicon Devices and Circuits. *IEEE Transactions on Computer-Aided Design, CAD-4* 436-451, 1985.

[5] S. Barnes, V. Merchant, F. Mahmud. Modulation of transmission gain by protons at the photoreceptor output synapse. *Proc. Natl. Acad. Sci. USA*, 90: 1008110085, 1993.

[6] M. Bouvier, M. Szatkowski, A. Amato, D. Attwell. The glial cell glutamate uptake carrier countertransports pH-changing anions. *Nature*, 360: 471474, 1992.

[7] A. L. Byzov, T.M. Shura-Bura. Electrical Feedback Mechanism in the Processing of Signals in the Outer Plexiform Layer of the Retina. *Vision Res.*, 26(1): 33-44, 1986.

[8] L. Cadetti, W. B. Thoreson. Feedback effects of horizontal cell membrane potential on cone calcium currents studied with simultaneous recordings. *J. Neurophysiol.*, 95: 19921995, 2006.

[9] M. Chun, H. Wässle. GABA-like immunoreactivity in the cat retina: Electron microscopy. *J. Comp. Neurol.*, 279(1): 5567, Jan. 1989.

[10] C. M. Davenport, P. B. Detwiler, D. M. Dacey. Effects of pH buffering on horizontal and ganglion cell light responses in primate retina: evidence for the proton hypothesis of surround formation. *J. Neurosci.*, 28:456464, 2008.

[11] S. H. DeVries. Exocytosed protons feedback to suppress the Ca^{2+} current in mammalian cone photoreceptors. *Neuron*, 32: 11071117, 2001.

[12] A. V. Dmitriev, S.C. Mangel. Electrical Feedback in the Code Pedicle: A Computational Analysis. *Journal of Neurophysiology*, 95: 1419-1427, 2006.

[13] K. Dunlap, G. D. Fischbach. Neurotransmitters decrease the calcium conductance activated by depolarization of embryonic chick sensory neurons. *Journal of Physiology - London* 317(Aug): 519535, October 1981.

[14] R. S. Eisenberg, M. M. Klosek, Z. Schuss. Diffusion as a chemical reaction: stochastic trajectories between fixed concentrations. *Journal of Chemical Physics*, 102: 17671780, 1995.

[15] I. Fahrenfort, M. Steijaert, T. Sjoerdsma, E. Vickers, H. Ripps, et al. Hemichannel-Mediated and pH-Based Feedback from Horizontal Cells to Cones in the Vertebrate Retina. *PLoS ONE*, 4(6): e6090. doi:10.1371/journal.pone.0006090.

[16] C.L. Gardner, J. R. Jones. Electrodiffusion model simulation of the potassium channel. *Journal of Theoretical Biology*. 291: 10-13, 2011.

[17] C. L. Gardner, W. Nonner, R. S. Eisenberg. Electrodiffusion model simulation of ionic channels: 1D simulations. *Journal of Computational Electronics* 3: 25-31, 2004.

[18] H. M. Gerschenfeld, M. Piccolino, J. Neyton. Feed-back modulation of cone synapses by L-horizontal cells of turtle retina. *J. Exp. Biol.* 89(0): 177192, 1980.

[19] C. Y. Guo, A. A. Hirano, S. L. Stella, M. Bitzer, N. C. Brecha. Guinea pig horizontal cells express GABA, the GABA-synthesizing enzyme GAD(65), and the GABA vesicular transporter. *Journal of Comparative Neurology*, 518(10): 16471669, May 2010.

[20] B. Hille. *Ion Channels of Excitable Membranes*. Sinauer Associates, Inc. Sunderland, MA, 2001.

[21] H. Hirasawa, A. Kaneko. pH changes in the invaginating synaptic cleft mediate feedback from horizontal cells to cone photoreceptors by modulating Ca^{2+} channels. *J. Gen. Physiol.*, 122: 657671, December 2003.

[22] U. Janssen-Beinhold, K. Schultz, A. Gellhaus, P. Schmidt, J. Ammermuller, R. Weiler. Identification and Localization of Connexin26 Within the Photoreceptor-Horizontal Cell Synaptic Complex. *Visual Neuroscience*, 18: 169-178, 2001.

[23] M. A. Johnson, N. Vardi. Regional differences in GABA and GAD immunoreactivity in rabbit horizontal cells. *Visual Neuroscience*, 15: 743753, 1998.

[24] M. Kamermans, I. Fahrenfort. Ephaptic interactions within a chemical synapse: hemichannel-mediated ephaptic inhibition in the retina. *Current Opinion in Neurobiology*, 14: 531-541, 2004.

[25] M. Kamermans, I. Fahrenfort, K. Schultz, U. Janssen-Blenhold. Hemichannel-Mediated Inhibition in the Outer Retina. *American Association for the Advancement of Science*, 292(5519): 1178-1180, 2001.

[26] M. Kamermans, D. Kraaij, H. Spekreijse. The dynamic charachteristics of the feedback signal from horizontal cells to cones in the goldfish retina. *Journal of Physiology*, 534.2: 489-500, 2001.

[27] M. Kamermans, H. Spekreijse. The feedback pathways from horizontal cells to cone: A mini review with a look ahead. *Vision Res.*, 39: 2449-2468, 1999.

[28] L.J. Klaassen, Z. Sun , M.N. Steijaert, P. Bolte, I. Fahrenfort, et al. Synaptic Transmission from Horizontal Cells to Cones Is Impaired by Loss of Connexin Hemichannels. PLoS Biol 9(7): e1001107. doi: 10.1371/journal.pbio.1001107, 2011.

[29] H. Kolb. Webvision, Chapter: Simple Anatomy of the Retina [Internet]. *Webvision*, accessed 2012 Oct 11. Available from: http://webvision.med.utah.edu/book/part-i-foundations/simple-anatomy-of-the-retina/.

[30] D. M. K. Lam, E. M. Lasater, and K.-I. Naka. γ-aminobutyric acid: A neurotransmitter candidate for cone horizontal cells of the catfish retina. *Proc. Natl. Acad. Sci. USA*, 75(12): 63106313, December 1978.

[31] D. M. K. Lam, Y. Y. T. Su, L. Swain, R. E. Marc, C. Brandon, J.-Y.Wu. Immunocytochemical localisation of L-glutamic acid decarboxylase in the goldfish retina. *Nature*, 278(5):565567, April 1979.

[32] S. C. Mangel, M. Ariel, J. E. Dowling. Effects of acidic amino acid antagonists upon the spectral properties of carp horizontal cells: circuitry of the outer retina. *J. Neurosci.*, 5: 28392850, 1985.

[33] R. E. Marc, W. K. Stell, D. Bok, D. M. K. Lam. GABA-ergic pathways in the goldfish retina. *J. Comp. Neurol.*, 182(2): 221245, November 1978.

[34] Y. Mori, J. W. Jerome, C. S. Peskin. A three-dimensional model of cellular electrical activity. *Bulletin of the Institute of Mathematics Academia Sinica*, 2: 367-390, 2007.

[35] Y. Mori, C. S. Peskin. A numerical method for cellular electrophysiology based on the electrodiffusion equations with internal boundary conditions at the membrane. *Communications in Applied Mathematics and Computational Sciences*, 4: 85-134, 2009.

[36] M. Murakami, Y. Shimoda, K. Nakatani, E. I. Miyachi, S. I. Watanabe. GABA-mediated negative feedback and color opponency in carp retina. *Japanese Journal of Physiology*, 32: 927935, 1982.

[37] M. Murakami, Y. Shimoda, K. Nakatani, E. I. Miyachi, S. I. Watanabe. GABA-mediated negative feedback from horizontal cells to cones in carp retina. *Japanese Journal of Physiology*, 32: 911926, 1982.

[38] R. Nelson, R. Pflug, S. M. Baer. Background-induced flicker enhancement in cat retinal horizontal cells. II. spatial properties. *Journal of Neurophysiology*, 64(2): 326340, August 1990.

[39] W. Nonner, R. S. Eisenberg. Ion permeation and glutamate residues linked by Poisson-Nernst-Planck theory in L-type calcium channels. *BioPhysical Journal*, 75: 17671780, 1995.

[40] Marco Piccolino. The feedback synapse from horizontal cells to cone photoreceptors in the vertebrate retina. *Progress in Retinal and Eye Research*, 14(1): 141196, 1995.

[41] B. Prodhom, D. Pietrobon, P. Hess. Direct measurement of proton transfer rates to a group controlling the dihydropyridine-sensitive Ca^{2+} channel. *Nature*, 329: 243246, 1987.

[42] E. A. Schwartz. Calcium-independent release of GABA from isolated horizontal cells of the toad retina. *J. Physiol.*, 323: 211227, 1982.

[43] E. A. Schwartz. Depolarization without calcium can release gammaaminobutyric acid from a retinal neuron. *Science*, 238(4825): 35355, Oct. 1987.

[44] N. Vardi, D. L. Kaufman, P. Sterling. Horizontal cells in cat and monkey retina express different isoforms of glutamic-acid decarboxylase. *Visual Neuroscience*, 11(1): 135142, 1994.

[45] J. Verweij, M. Kamermans, H. Spekreijse. Horizontal Cells Feed Back to Cones by Shifting the Cone Calcium-Current Activation Range. *Vision Res.*, 36(24): 3943-3953, 1996.

[46] J. P. Vessey, A. K. Stratis, B. A. Daniels, N. D. Silva, M. G. Jonz, M. R. Lalonde, W. H. Baldridge, S. Barnes. Proton-mediated feedback inhibition of presynaptic calcium channels at the cone photoreceptor synapse. *The Journal of Neuroscience*, 25(16): 41084117, 2005.

[47] Wikipedia contributors. Neuron [Internet]. *Wikipedia, The Free Encyclopedia*, accessed 2012 Oct 10. Available from: http://en.wikipedia.org/wiki/Neuron.

[48] Wikipedia contributors. Quantitative models of the action potential [Internet]. *Wikipedia, The Free Encyclopedia*, accessed 2012 Oct 11. Available from: http://en.wikipedia.org/wiki/Quantitative_models_of_the_action_potential.

APPENDIX A

CELL MEMBRANE SURFACE CHARGES

We now give a more general discussion on possible ways to approximate the integral from 2.21 in subsection 2.3. To simplify notation, we will only consider the intracellular $(+)$ side of the membrane since the equations on the extracellular side are identical. Define the normalized charge density for the ith ionic species as

$$\bar{\sigma}_i = \frac{\sigma_i}{q_i n_{b,i} l_D} = \int_0^\infty \left(\frac{n_i(z)}{n_{b,i}} - 1 \right) \, dz \approx \int_0^\infty \left(\exp\{-u_i e^{-z}\} - 1 \right) \, dz \tag{A.1}$$

where $z = x/l_D$ and $u_i = q_i(\phi(0) - \phi_b)/(k_B T)$. Our physical approximation (A) is based on the fact that the charge layers decay exponentially away from the membranes with a characteristic length scale of a Debye length:

$$\bar{\sigma}_i \approx \frac{n_i}{n_{b,i}} - 1 = e^{-u_i} - 1 \quad (A) \tag{A.2}$$

which results in the approximation $\sigma_i = q_i l_D (n_i - n_{b,i})$.

The approach taken by Mori et al. in [34] results in the twice linearized approximation (M) given by

$$\bar{\sigma}_i \approx -\int_0^\infty u_i e^{-z} \, dz = -u_i \quad (M) \tag{A.3}$$

which is also the linearized version of (A).

For larger potential magnitudes $|u_i|$, we can evaluate the integral from A.1 using the exponential integral special function, resulting in a nearly exact approximation (PB). Define the function

$$f(u) = \int_0^\infty \left(\exp\{-u e^{-z}\} - 1 \right) \, dz = -E_1(u) - \ln(u) - \gamma_E \tag{A.4}$$

where $E_1(\eta) = \int_\eta^\infty (e^{-t}/t) \, dt$ and γ_E is the Euler-Mascheroni constant. This function is monotonically decreasing and can therefore be inverted to obtain u_i from $\bar{\sigma}_i$, which defines the (PB) approximation. This can be achieved by generating a table of values containing u and $f(u)$ for several values of u in a desired range. Given a value of $\bar{\sigma}_i$, the table is searched to find the interval containing $\bar{\sigma}_i$ and then $u_i = f^{-1}(\bar{\sigma}_i)$ is evaluated using linear interpolation in this interval. The membrane values for the particle densities would then be

$$n_i = n_{b,i} \exp\{-u_i\}. \tag{A.5}$$

The approximations (A) and (M) are compared with this nearly exact numerical Poisson-Boltzmann solution (PB) in Figure A.1.

To test the approximation (A), we compared the IV curves resulting from approximations (A) and (PB). We found that the IV curves for both cases were identical to within a line width, since for this problem, $|u_i| \ll 1$. However, the (PB) approximation is more expensive to compute so we used approximation (A) for all simulations.

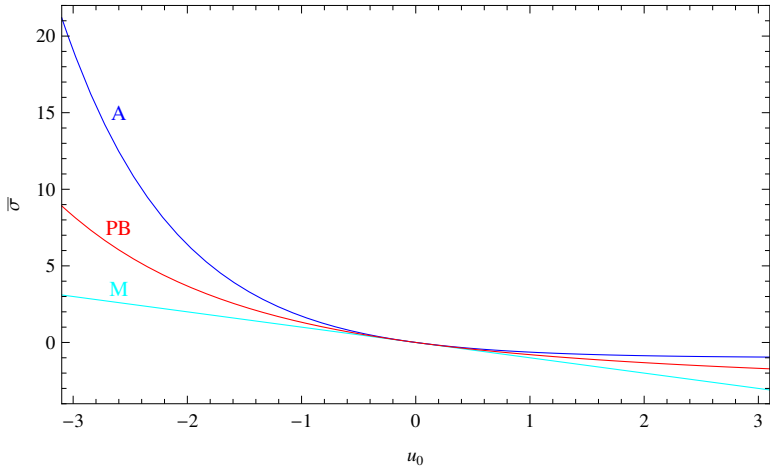

Figure A.1: Comparison of the nearly exact Poisson-Boltzmann solution (PB) for σ_i vs. u_i with the approximations (A) and (M).